國立臺灣大學理學院物理學研究所

碩士論文

Department of Physics
College of Science
National Taiwan University
Master's Thesis

三光子高速旋轉盤顯微術應用於腦成像

Three-photon high-speed spinning disk microscopy for brain imaging

廖于碩

Yu-Shuo Liao

指導教授：朱士維 博士

Advisor: Shi-Wei Chu, Ph.D.

中華民國 113 年 04 月

April, 2024

doi:10.6342/NTU202400835

國立臺灣大學碩士學位論文
口試委員會審定書
MASTER'S THESIS ACCEPTANCE CERTIFICATE
NATIONAL TAIWAN UNIVERSITY

三光子高速旋轉盤顯微術應用於腦成像

Three-photon high-speed spinning disk microscopy for brain imaging

本論文係 廖于碩（R10222090）在國立臺灣大學物理所完成之碩士學位論文，於民國 113 年 4 月 1 日承下列考試委員審查通過及口試及格，特此證明。

The undersigned, appointed by the Department of Physics on April 1st, 2024, have examined a Master's thesis entitled above presented by Yu-Shuo Liao (R10222006) candidate and hereby certify that it is worthy of acceptance.

口試委員 Oral examination committee:

朱士維	楊尚達	謝佳龍
（指導教授 Advisor）		

doi:10.6342/NTU202400835

致謝

轉眼間，也在實驗室待了將近5年了。在這一段時間內，我深深感謝許多給予指導、協助和陪伴的人們。首先，要感謝朱士維老師，自大學時期加入實驗室以來，他給予我們很大的自由度並鼓勵我們進行許多嘗試。這段時間，我得以進行許多有趣的實驗，深入瞭解神經光學成像領域，並有幸接觸到眾多相關實驗室，甚至有機會與不同的團隊合作。

此外，我要感謝冠傑、旭峰在他們於此研究上的幫忙，以及當遇到困難時的討論與建議。我還要感謝實驗室的其他夥伴們，Kentaro、 德心、品壬、庭禎、尹慈、致嘉、子婷、Mor Pal、俞安、重名、品淳、奕蓁、和家、東翰，在這一段時間內除了很高興能與你們一起共事外，研究之餘一起玩桌遊、吃晚餐、出去玩等美好時光，也使實驗室的氣氛歡樂不少。

此外，我還要感謝萊斯大學的Kono老師，以及實驗室的Jacques、Andrey、Natsumi和心月等人，他們在我在萊斯大學進行實驗時給予了許多的協助。同時也要感謝在休士頓認識的朋友和長輩們，豐富了我在這座城市的生活經歷。

最後，我要感謝我的家人，我的父母與弟弟們，在這一段時間無條件的支持與鼓勵。我想起在休士頓時聽到的一句俗語: If you want to go fast, go alone. If you want to go far, go together. 這也是我這一段時間來的體悟。

doi:10.6342/NTU202400835

中文摘要

在神經科學的研究中，徹底地了解大腦結構性與功能性的迴路是至關重要的目標。而高速深組織的活體腦成像是達到此目標的必要條件之一。近年來，隨著雷射技術的發展，結合高速成像技術（如光片、旋轉盤或多焦點陣列掃描顯微術）的雙光子激發螢光顯微鏡被研發出來，並應用在生物樣本上。這些技術使得對於小型模式動物的活體高速深組織光學腦成像變得逐漸可行。然而，儘管相比於雙光子激發，三光子激發在深組織有其優勢，但在目前的文獻中卻很少有高速三光子的系統被成功開發。

在本研究中，我們利用客製化的旋轉盤結合可調波長的高功率飛秒雷射系統，展示了首個三光子旋轉盤顯微鏡，我們達到了接近300 Hz的幀率進行三光子成像，為首個超過100 Hz 幀率的三光子顯微鏡。我們對不同的樣本進行成像，包含綠色螢光球、固定的小鼠腦片與活體的果蠅進行腦成像，以展示其能力。在實驗中我們實現了以3毫秒的曝光時間對微流道晶片中的流動螢光球進行高速成像。而在對老鼠與果蠅的腦成像實驗則顯示出，相比於雙光子旋轉盤成像，三光子旋轉盤成像具有更低的訊號衰減率。我們的研究實現了目前最高速的三光子成像，提供了一種可行的三光子高速成像系統。

關鍵字： 三光子顯微鏡、多光子顯微鏡、旋轉盤顯微鏡、腦成像、訊號衰減

doi:10.6342/NTU202400835

Abstract

Achieving a comprehensive understanding of the brain's structural and functional circuits is a crucial goal in neuroscience. To address this need, high-speed volumetric imaging of emergent properties within the connectomes of living animals is essential. Advances in laser techniques have enabled deep tissue imaging of the brain at high speed by combining two-photon excitation with rapid microscopy methods such as light-sheet, spinning disk, or multifoci array scanning microscopy. Despite the potential for improved imaging depth compared to two-photon excitation, high-speed three-photon imaging remains relatively scarce in the literature.

In this study, we utilize a customized spinning disk unit combined with a wavelength-tunable high-power femtosecond laser to showcase the three-photon microscopy at a frame rate of ~300 Hz, marking a significant milestone in achieving three-photon microscopy above the 100 Hz regime. We demonstrate its versatility by imaging various samples, including green fluorescent beads, *in vivo Drosophila* brains, and fixed mouse brains. Our experimental setup achieves three-photon high-speed imaging with an exposure time of only 3 ms for floating fluorescent beads inside a microfluidic chip. Furthermore, our brain imaging findings reveal that three-photon spinning disk imaging exhibits a lower attenuation rate compared to its two-photon spinning disk counterpart. Our work paves the way for utilizing three-photon excitation in high-speed deep tissue imaging applications.

Key words: three-photon microscopy, multiphoton microscopy, spinning disk microscopy, brain imaging, signal attenuation

doi:10.6342/NTU202400835

Contents

doi:10.6342/NTU202400835

List of Figures

doi:10.6342/NTU202400835

List of Tables

doi:10.6342/NTU202400835

Ch1. Introduction

Understanding how the brain works to implement complex behaviors such as moving, learning, memorizing, and forgetting remains a central challenge for humans. The questions such as “What is the biological basis of consciousness?”, “How are memories stored and retrieved” remained the top question for scientists during the past few decades (Kennedy & Norman, 2005). To study these questions, not only the “hardware”---structural connection of neurons, but also the “software”---functional connectome of the brain needs to be observed (Huang et al., 2021). Hence, the functional imaging tool for the brain is crucial. In this chapter, I will briefly discuss functional imaging tools for studying the brain and why developing optical microscopy that allows high-speed deep tissue imaging beyond cellular resolution is critical for neurobiology.

1.1 Tools for Neuroimaging: The Advantage of Optical Microscopy

In recent decades, various techniques such as positron emission tomography (PET), functional magnetic resonance imaging (fMRI), functional ultrasound imaging (fUS), electrophysiology, electroencephalography (EEG), magnetoencephalography (MEG), and optical microscopy have emerged for studying and understanding the complexities of the brain. Each technique possesses its own set of advantages and limitations concerning factors like spatial resolution, temporal resolution, and penetration depth.

doi:10.6342/NTU202400835

Among the above techniques, electrophysiology and EEG directly measure the electrical signal of neurons, which discovery can be traced back to 1780 to Galvani's study on bioelectricity (Whittaker, 2018). After 1939, Hodgkin and Huxley first recorded the intracellular action potential from a neuron (Hodgkin & Huxley, 1939), and various techniques such as electrodes have been used to study the electrophysiology of neurons. The advantage of electrophysiology is its high sensitivity and temporal resolution, allowing scientists to conduct detailed examination of the mechanisms underlying neural signaling, including the generation and propagation of action potentials. However, it faces several challenges, including invasiveness, limited spatial resolution, and confinement to small areas (Scanziani & Häusser, 2009).

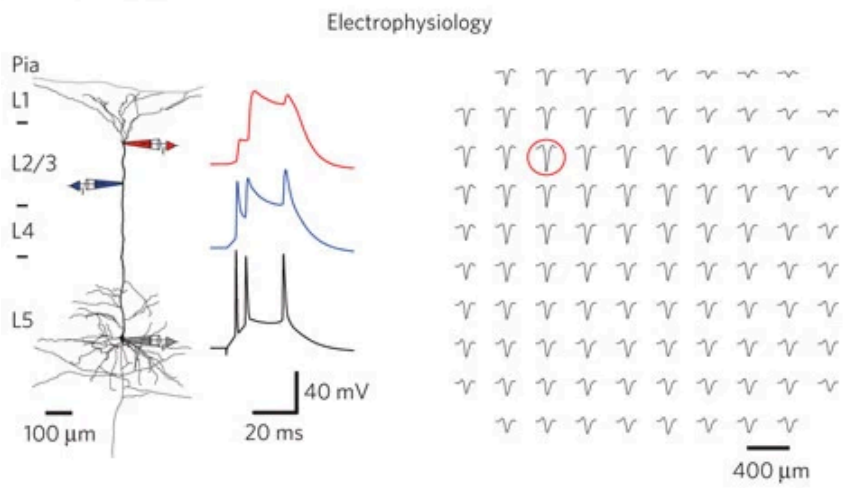

Figure 1: Illustration of electrophysiology measurement of using (a) three simultaneous patch-clamp records calcium spikes of pyramidal neurons and (b) using an electrode array to capture the spatial information of functional signal of neurons. Figures are reproduced with permission from (Scanziani & Häusser, 2009).

On the other hand, EEG captures large-scale electrical signals from the nervous system by detecting voltage differences between electrodes placed on the scalp, offering real-time insights into brain function and various neurological conditions. MEG records the weak magnetic fields induced by synchronized neuronal currents. Both techniques

doi:10.6342/NTU202400835

boast high temporal resolution and are non-invasive. However, their relatively poor spatial resolution, typically measured in centimeters, and the absence of depth information pose challenges in precisely locating the source of neural activity within the brain, especially when studying deeper brain structures (Glover, 2011; He et al., 2011).

PET, fMRI, and fUS indirectly acquire neural activity by imaging blood flow through the injection of a small amount of radioactive substance, nuclear magnetic resonance, and direct ultrasound detection, respectively. These techniques can provide three-dimensional (3D) imaging throughout the entire human brain (PET/fMRI) or mouse brain (fUS). However, due to their indirect measurement of neural signals as well as insufficient spatial and temporal resolution, they are unable to discern individual neurons and their ionic/electric dynamics (Glover, 2011).

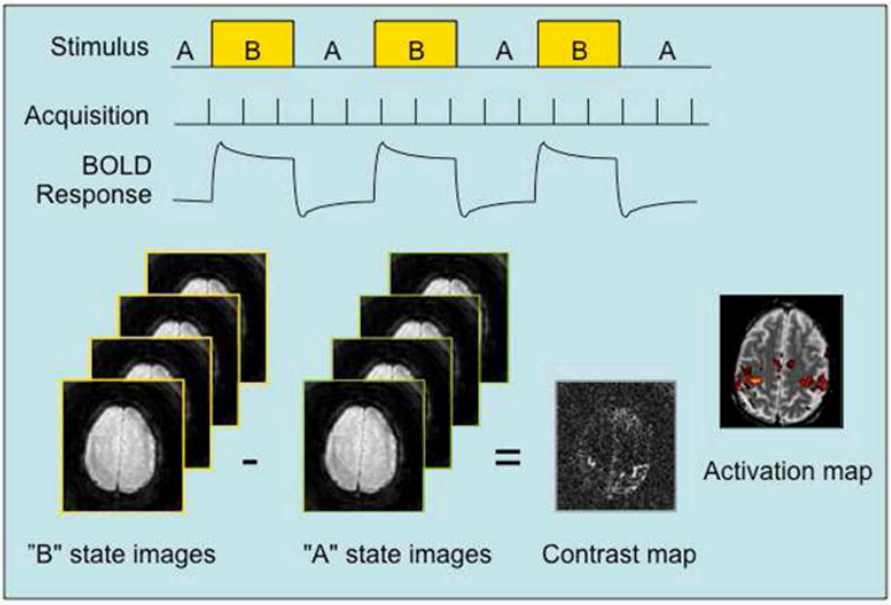

Figure 2: Illustration of working principle of fMRI. The figure is reproduced with permission from (Glover, 2011)

doi:10.6342/NTU202400835

In recent years, on the other hand, advancements in optical imaging techniques have facilitated the exploration of connectomes with high spatiotemporal resolution across the entire brain of small animals. These methods enable the capture of functional signals in each neuron while simultaneously observing a large number of neurons, providing insights into the "emerging" physiological behaviors at cellular to sub-cellular resolution (Huang et al., 2021).

In contrast to EEG, MEG, PET, fMRI and fUS, optical imaging falls short in penetration depth. However, it offers superior spatial resolution, typically reaching sub-micrometer levels, and even achieving 2–100-fold enhancements through super-resolution methods (Sigal et al., 2018). This heightened spatial resolution allows optical microscopy to delve into at least sub-cellular and, in some cases, down to the synapse level—far surpassing the capabilities of current medical imaging modalities.

Recent studies have utilized electron microscopy (EM) to investigate the structural connectomes of substantial brain volumes (Furuta et al., 2022; Kornfeld & Denk, 2019) and even the entire *Drosophila* brain (Zheng et al., 2018) at the nanometer resolution. However, the current impossibility of *in vivo* functional imaging using EM highlights the unique advantage of optical microscopy in achieving such dynamic studies.

doi:10.6342/NTU202400835

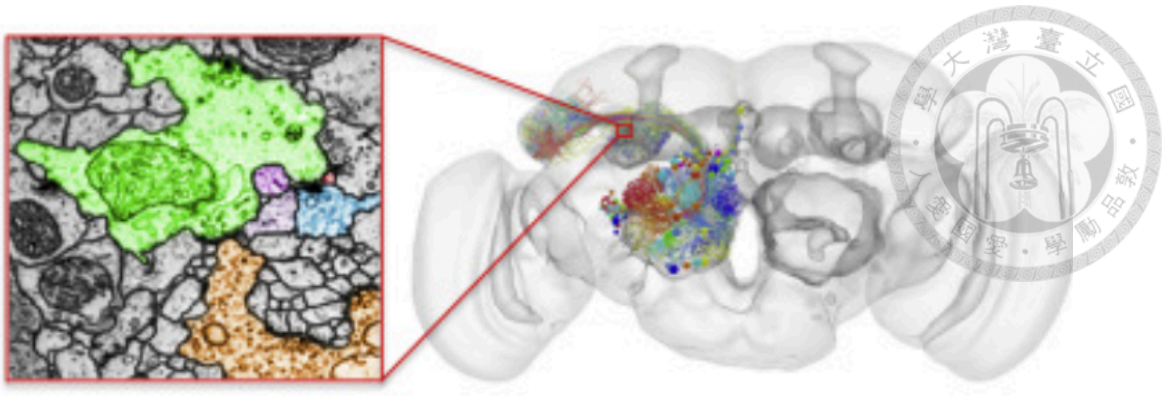

Figure 3: EM imaging of a complete adult Drosophila brain. The figure is reproduced with permission from (Zheng et al., 2018).

Hence, in the upcoming chapter, I will delve into optical methods for neural studies, addressing their existing challenges, and focusing on limitations related to penetration depth and imaging speed. Furthermore, I will explore strategies to overcome these obstacles and push the boundaries of current capabilities.

Imaging method	Electrophysiology	EEG	PET	fMRI	EM	Optical Microscopy
Functional imaging	Yes	Yes	Yes	Yes	No	Yes
Spatial Resolution	~ μm	~ cm	~ mm	~ mm	~ sub nm	~ sub μm
Temporal resolution	~ ms	~ms	~ minute	~second	X	~ ms
Imaging depth	near-surface	~surface	~ whole human brain	~ whole human brain	~ surface	~ mm

Table 1: Comparison of the main brain imaging methods for studying the structure and function of the brain.

doi:10.6342/NTU202400835

1.2 Optical microscopy for brain imaging

Biological discoveries have frequently been intertwined with advancements in microscopy. In the 17th century, the introduction of the optical microscope revolutionized the study of biological specimens, allowing examination at the microscale level. As microscopy techniques advanced, magnification technology evolved to a point where it could discern the existence of cells, culminating in the formalization of cell theory in the mid-nineteenth century (Müller-Wille, 2010).

Subsequently, in the late 19th century, the discovery of the Nissl stain, Golgi stain, and the subsequent research by Cajal ushered in a new era of studying neurons through optical microscopy, leading to the formulation of the neuron doctrine. Alongside these developments, the evolution of microscopy continued with innovations such as the phase-contrast microscope by Fritz Zernike in 1933 (Zernike, 1942), the confocal microscope by Marvin Minsky in 1957 (Minsky, 1957), and nonlinear optical microscopy techniques like multi-photon fluorescence microscopy, second or third harmonic generation, coherent anti-Stokes Raman scattering (CARS) (Duncan et al., 1982), stimulated Raman scattering (SRS) (Freudiger et al., 2008), as well as the refinement of various staining materials like green fluorescent protein (GFP) and its derivatives (Shimomura et al., 1962), all contributing significantly to the advancement of neuroscience understanding (Araki, 2017).

To comprehend the working principle of the brain and its implementation of complex behaviors, it is imperative to observe not only the hardware—the structural circuitry of the neural network, but also the software—the functional connectome of neurons. Meeting these requirements

doi:10.6342/NTU202400835

necessitates volumetric imaging of emergent properties from connectomes in living animals at high speeds. Consequently, techniques capable of enhancing penetration depth to encompass larger brain volumes while maintaining high frame rates to capture functional signals are crucial in neuroscience. In the subsequent sections, I will focus on optical imaging techniques tailored for deep tissue imaging and high-speed imaging, respectively.

1.3 Deep tissue imaging — Multiphoton fluorescence microscopy

Deep tissue *in vivo* imaging poses a significant challenge due to the considerable scattering and absorption of excitation light by biological tissue (Juan M. Bueno & Chu, 2022). The power of excitation light decreases exponentially with depth in biological tissue, as described by the equation:

$$\mathrm{P(z)} = \mathrm{P}_0 \cdot \exp\left(-\mathrm{z}/l_e\right)$$

where P(z) is the power of excitation at depth z, P_0 is the power of excitation at the surface and l_e is the effective attenuation length (EAL). This parameter is attributed to absorption and tissue scattering, as described by the formula below (Horton et al., 2013):

$$\frac{1}{l_e} = \frac{1}{l_a} + \frac{1}{l_s}$$

Where l_e is the EAL, l_a is the absorption length, and l_s is the scattering mean free path cause by tissue. The absorption is typically dominated by melanin and blood (Oxygenated Hemoglobin, HbO2 and Deoxygenated Hemoglobin, Hb) when wavelength is below 1 μm and dominated by water when wavelength is above 1μm (Keiser, 2022). Tissue scattering, primarily due to Rayleigh scattering, is inversely proportional to the fourth power of the wavelength, leading to

doi:10.6342/NTU202400835

weaker scattering effects with longer excitation wavelengths. Advances in two-photon (2P) excitation microscopy have enhanced penetration depth for scattering samples (Diaspro et al., 2005), while extending excitation wavelengths and leveraging nonlinear absorption processes have facilitated deeper penetration and intrinsic optical sectioning.

Despite these advancements, certain biological studies face limitations. For instance, *in vivo Drosophila* labeled with GFP struggles to achieve depths beyond 100 μm with two-photon excitation at 920 nm, mainly due to strong scattering and aberrations introduced by the tracheal system (Hsu et al., 2019). Conversely, three-photon (3P) excitation at 1300 nm has demonstrated effectiveness in reaching depths of up to 200 μm, facilitating imaging down to the base of the brain (Figure 4a). One of the analyses reveals an attenuation length of 104 μm for 2P excitation (920 nm) and 151 μm for 3P excitation (1300 nm) in Gal4-elav.L/CyO × UAS-EGFP Drosophila specimens (Hsu et al., 2019).

In the *in vivo* mouse brain, similarly, standard scanning two-photon microscopy is limited to approximately 600 μm (Xiao et al., 2023). In contrast, scanning three-photon microscopy at 1300 nm or 1700 nm excitation wavelengths has shown significantly improved penetration depths, reaching approximately 1200 μm (Streich et al., 2021) and 2100 μm (Liu et al., 2019) for mouse brain imaging respectively.

doi:10.6342/NTU202400835

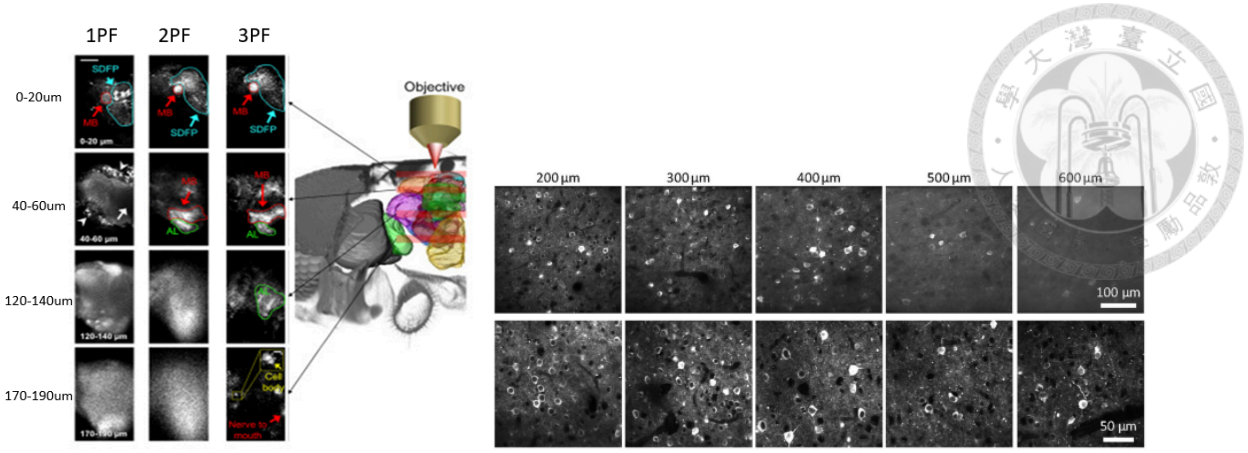

Figure 4: (a) Comparison of 1P, 2P, and 3P imaging of living *Drosophila* brain. The figure is reproduced with permission from (Hsu et al., 2019). (b) Comparison of 2P and 3P imaging of Emx1-IRES-Cre;CaMK2a-tTA;Ai94 mouse at different depth. The figure is reproduced with permission from (Takasaki et al., 2020).

Figure 5, reproduced from (Au - Hontani et al., 2022), illustrates the calculated effective attenuation length (EAL) and the experimental measurements in the neocortex of the mouse brain. The experimental data reveals that the EAL in the *in vivo* cortex of mouse brains is approximately 152~158 µm at 920 nm and 305~319 µm at 1300 nm, respectively (Wang et al., 2017). In the white matter region, the EAL is reported to be around 73~119 µm at 920 nm and 99~125 µm at 1300 nm (Wang et al., 2017).

doi:10.6342/NTU202400835

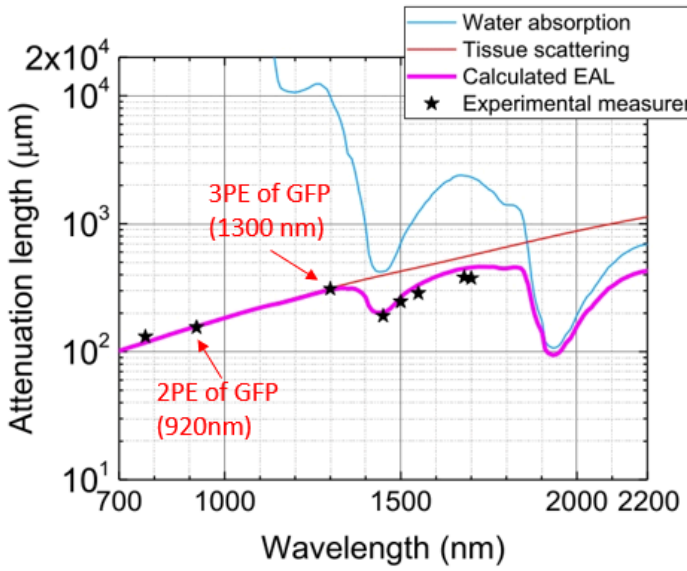

Figure 5: Effective attenuation length in the neocortex of the mouse brain. The figure is reproduced with permission from (Au - Hontani et al., 2022)

1.4 Deep tissue functional imaging — High-speed multi-photon microscopy

To investigate the functional connectome of the brain, it's essential to conduct high-speed multiphoton imaging, enabling deep tissue *in vivo* functional high-speed imaging to capture the dynamic of neurons. Over the past two decades, numerous high-frame-rate 2P microscopy techniques for *in vivo* functional imaging have been developed (Wu et al., 2021). These techniques span from point scanning methods achieving frame rates from Hz to sub-hundred Hz, primarily limited by the scanning speed of Galvo mirrors, to high-speed imaging strategies capable of reaching up to kHz frame rates through various techniques such as spatial multiplexing (multi-foci array)(Zhang et al., 2019), where the intrinsic limit is determined by the

doi:10.6342/NTU202400835

laser's repetition rate. Other approaches include spinning disk microscopy (Otomo et al., 2015; Otomo et al., 2020), widefield temporal focusing (Dana et al., 2014; Schrodel et al., 2013), and light-sheet microscopy (Maioli et al., 2020; Truong et al., 2011; Wolf et al., 2015), the speed limit is constrained by widespread illumination across a large area, leading to a reduction in excitation intensity and thus signal intensity.

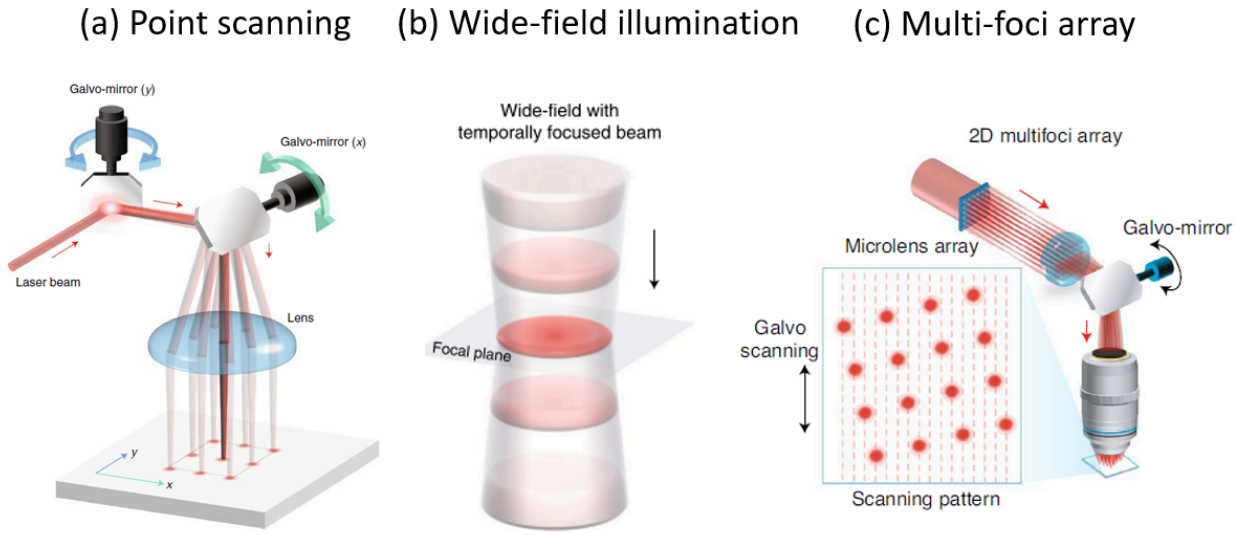

Figure 6: Different 2P imaging techniques. (a) Point scanning (b) Wide-field illumination (c) Multu-foci array.The figure is reproduced with permission from (Wu et al., 2021).

Although various types of high-speed 2P fluorescence microscopes have been developed, high-speed 3P imaging systems remain relatively scarce in the existing literature. The limited availability of high-speed 3P systems is primarily attributed to the significantly smaller 3P absorption cross-section compared to 2P absorption. As a consequence, 3P microscopy often requires higher pulse energy than 2P microscopy to achieve comparable fluorescence levels, necessitating pulsed lasers with lower repetition rates (~1 MHz for 3P versus 80 MHz for 2P) (Au - Hontani et al., 2022) to maintain average power within sample heat accumulation limits.

doi:10.6342/NTU202400835

Consequently, single-point scanning 3P systems struggle to achieve frame rates easily attained by 2P systems (sub-hundred Hz). For example, the speed limit of point-scanning 3P with a 1 MHz repetition rate laser is approximately 15 frames per second for a 256x256 pixels scan. On the other hand, in widefield illumination techniques such as light-sheet or temporal focusing microscopy, the larger illuminated area reduces excitation intensity, leading to a cubic decrease in fluorescence signal and requiring longer exposure times. Below, I will briefly review current high-speed three-photon microscopy research.

The three-photon *in vivo* mouse brain imaging have been conducted in 2017 using 3P point scanning microscopy at 256*256 pixels, achieving approximately 8.5 Hz (Ouzounov et al., 2017). Presently, 3P point scanning with smaller pixel number 50*50 pixels has achieved a frame rate of approximately 78 Hz (Weisenburger et al., 2019).

To enhance speed, camera-based three-photon imaging was pioneered by Rowlands et al. in 2017 (Rowlands et al., 2017) and Toda et al. (Toda et al., 2017). They utilized 3P widefield imaging excitation by temporal focusing techniques at 1300 nm and 1060 nm, respectively. Rowlands employed a regenerative amplifier with an optical parametric amplifier (OPA) system to excite quantum dots injected into a mouse vein, achieving 5 s integration times with a ~250 μm diameter field of view (Rowlands et al., 2017). Toda utilized a Yb-fiber chirped pulse amplifier (CPA) system, achieving exposure times of 100 ms and 30 ms on 1 μm aggregated fluorescent beads and DAPI-stained fixed mouse brain tissue, respectively, with a field of view of 30x30 μm (Toda et al., 2017).

doi:10.6342/NTU202400835

In 2018, Escobet-Montalbán et al. demonstrated the first three-photon excitation light-sheet fluorescence microscopy using a Ti: sapphire ultrashort pulsed laser at a 1,000 nm wavelength, imaging blue fluorescing microspheres and 450 μm diameter cellular spheroids (Escobet-Montalbán et al., 2018). The primary focus of their study was to showcase improved optical sectioning capabilities compared to traditional two-photon light-sheet microscopy techniques. Thus, they did not provide specific information regarding the imaging speed in their study.

However, all the research mentioned above falls below the 100 Hz frame rate threshold, rendering it inadequate for capturing fast neural activities that can be labeled by millisecond-scale voltage indicators (Bando et al., 2019) or recently developed fast and sensitive GCaMP calcium indicators (Zhang et al., 2023). These indicators have garnered significant attention from neuroscience communities due to their ability to provide insights into high-resolution measurements of spiking and synaptic activity in neuronal populations. Hence, in this work, we are going to push the speed limit of 3P imaging techniques into the hundred Hz regime.

3P imaging method	**Point scanning** (Dimitre G Ouzounov, 2017)	**Temporal focusing** (Keisuke Toda, 2017)	**Light-sheet** (Escobet-Montalbán,2018)
Laser/ Repetition rate	noncolinear optical parametric amplifier (NOPA) at 1300nm, 500mw, 400kHz	Yb-fiber laser, 92-fs 9.0-μJ at 1060-nm, 200 kHz.	Ti:sapphire laser at 1,000nm , 140 fs, 80MHz
Sample/Exposure time/FOV	GCaMP6-labeled mouse brain / 8.49 Hz /(256 256 pixels), 200*200 μm	Fixed mouse brain tissue/30 ms/~30*30um	HEK 293 T17 labeled with PUREBLU dye/ ~250um*250um

Table 2: Current work of high-speed 3P microscopy

doi:10.6342/NTU202400835

1.5 Our solution — Three-photon spinning disk microscopy

In the previous section, we discussed the bottlenecks encountered in achieving high-speed 3P imaging using single-point scanning and wide-field illumination techniques, attributed to the low repetition rate of pulse lasers and insufficient intensity at the focal plane, respectively. Consequently, we aim to leverage a technique that bridges the gap between these approaches—spinning disk microscopy.

Spinning disk microscopy employs hundreds to thousands of microlenses and pinholes to divide a single beam into smaller beams, which scan through the sample simultaneously (Oreopoulos et al., 2014). Unlike uniformly illuminating the entire layer, the spinning disk system excites multiple points simultaneously while spinning at high speed, effectively scanning through the entire layer and resulting in higher intensity for each point. This unique characteristic offers a significant advantage in three-photon widefield imaging. Moreover, the pinholes in the system and the non-linear effect cause from multiphoton excitation efficiently filter out scattered light and enhancing the signal-to-background ratio (Shimozawa et al., 2013) which make it generate a "virtual lightsheet". Consequently, spinning disk systems are well-suited for 3P high-speed imaging on biological samples.

In Chapter 2, we will delve into the principles underlying three-photon spinning disk microscopy techniques, while Chapter 3 will elaborate on the optical setup of our system and the optimization process. Chapter 4 will encompass the experiments conducted, encompassing power-dependent tests, demonstrations of high-speed imaging, and experiments on biological

doi:10.6342/NTU202400835

samples, followed by discussions. Finally, Chapter 5 will offer a conclusion and outline potential future research.

doi:10.6342/NTU202400835

Ch2. Principle of Techniques for Three-photon Spinning Disk Microscopy

In this chapter, I will discuss the principle of each technique the three-photon spinning disk system applies, including the physics of three-photon excitation and the modality of spinning disk microscopy.

2.1 Principle of three-photon excitation microscopy

The three-photon excitation process is a nonlinear optical phenomenon harnessed in fluorescence microscopy. In contrast to single- or two-photon excitation, where one or two photons, respectively, excite a fluorophore, the three-photon excitation process involves the simultaneous absorption of three lower-energy photons to achieve an excited state. Figure 7 below illustrates the Jablonski diagram, depicting one-, two-, and three-photon excitation processes.

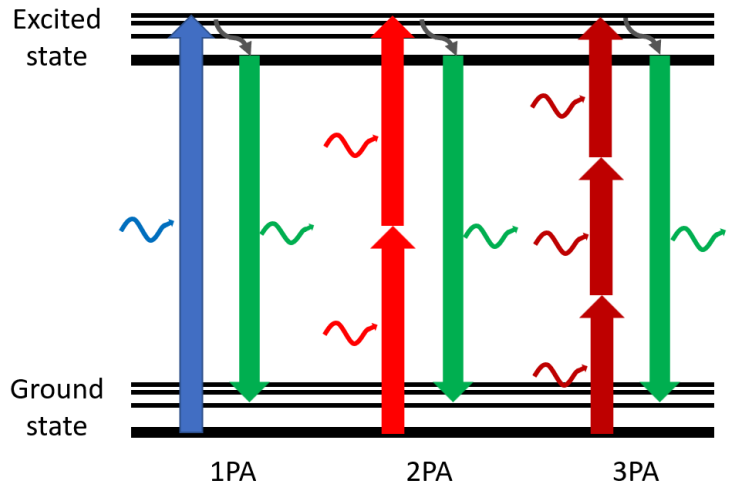

\

Figure 7 : The Jablonski diagram illustrating of one, two, and three-photon absorption process.

doi:10.6342/NTU202400835

The principle underlying three-photon excitation is based on the requirement that the energy of three photons must combine to equal the energy necessary to excite a fluorophore. Consequently, three-photon excitation offers enhanced tissue penetration capabilities due to longer excitation wavelengths and higher-order nonlinear excitation processes. However, it's important to note that the action cross-section of three-photon excitation, the ability of a molecule or fluorophore to absorb three photons simultaneously, is much smaller than that of two-photon absorption. For example, the 2P action cross-section of wtGFP is 21.6 x 10^{-50} cm^4s/photon and is 15.9 x 10^{-84} cm^6 $(s/photon)^2$ for 3P absorption. This necessitates the utilization of pulsed lasers with high photon flux to achieve efficient excitation. The time-averaged fluorescence photon flux has been derived by Cheng et al (Cheng et al., 2014):

$$\left\langle F^{(n)}(t)\right\rangle = \frac{1}{n}\frac{g_p^{(n)}}{(f\tau)^{n-1}}\phi\eta\sigma_n C n_0 \frac{a_n (NA)^{2n-4}\langle P(t)\rangle^n}{8\pi^{3-n}\lambda^{2n-3}}$$

Parameter	Description
n	number of photons absorbed
<P(t)>	time-average excitation power
f	laser repetition rate
τ	laser pulse width
φ	system collection efficiency
C	concentration of the fluorophore
η	fluorescence quantum efficiency
σ_n	n-photon absorption cross-section
ησ	action cross-section
λ	excitation wavelength

doi:10.6342/NTU202400835

a_n	constant, where a2=64, a3=28.1
NA	numerical aperture of the imaging system
n_0	the refractive index of the sample media
$g^{(n)}_p$	nth-order temporal coherence of the excitation source: $g^{(n)}_p$=0.0664, $g^{(n)}_p$= 0.51 for Gaussian temporal profile pulse

Table 3 : Parameter related to the time-averaged fluorescence photon flux of multi-photon excitation.

From this equation, we can deduce that the multi-photon microscopy signal can be enhanced by a factor of $(I)^n/(\tau R)^{n-1}$ where I is the average excitation intensity, τ represents the pulse width, n indicates the number of photons, and R denotes the laser repetition rate. Given that the 3P absorption cross-section is significantly smaller than that of 2P absorption, 3P microscopy necessitates higher pulse energy compared to 2P microscopy. To maintain the excitation intensity within the heat limit without thermally damaging the sample, 3P microscope typically requires a pulsed laser with a lower repetition rate, equal to or below 1 MHz for 3P compared to the commonly used 80 MHz for 2P microscopy.

2.2 Principle of spinning disk confocal scanning unit

Traditional laser scanning microscope operates by directing a single laser beam across the specimen plane, scanning point by point. However, this method faces limitations in image acquisition speed due to the precise control needed for galvanometer mirrors and the pixel dwell time. As a result, acquisition speeds typically range from half a second to two seconds per image. Yet, to capture millisecond dynamic events in living cells, faster imaging techniques are necessary.

doi:10.6342/NTU202400835

Spinning disk confocal microscopy (SDCM) offers a solution to this challenge. Invented by Mojmír Petráň in 1968 (Petráň et al., 1968), the first SDCM utilized a rotating scanning Nipkow disk to construct a double-sided SDCM. This setup enabled multiple-point illumination coupled with detection in reflected light confocal imaging, achieving a scanning speed of the entire field of view up to 120 times per second.

In 1988, G. Q. Xiao et al. further advanced SDCM technology by developing a single-sided spinning disk confocal microscope. This innovation utilized the same set of pinholes for both illumination and detection, capable of generating 640 frames per second by illuminating thousands of pinholes on a rotating disk simultaneously. (Xiao et al., 1988).

Early single-disk SDCM designs suffered from poor illumination efficiency, typically around 4% transmission. To overcome this limitation, dual-disk technology was introduced. In this setup, each pinhole on the Nipkow disk is matched with a microlens on another disk, mounted together on a motor shaft with a gap matching the focal length of the microlenses. This substantially enhances the illumination efficiency, by up to 40%. The patent for this technology was licensed to Yokogawa Electric Corporation in the 1990s (Oreopoulos et al., 2014).

Figure 8 from the Yokogawa website illustrates the fluorescence imaging process of the Yokogawa spinning disk unit. The laser excitation beam is introduced into the microlens array, separating it into hundreds of smaller beams. These beams pass through a dichroic mirror and each pinhole individually, filling the back aperture of the objective and focusing on the imaging plane. Fluorescence emission is collected through the objective, focused back onto the pinhole

doi:10.6342/NTU202400835

disk to block out-of-focus signals, reflected by the dichroic mirror, passed through the emission filter and tube lens, and finally collected by the camera.

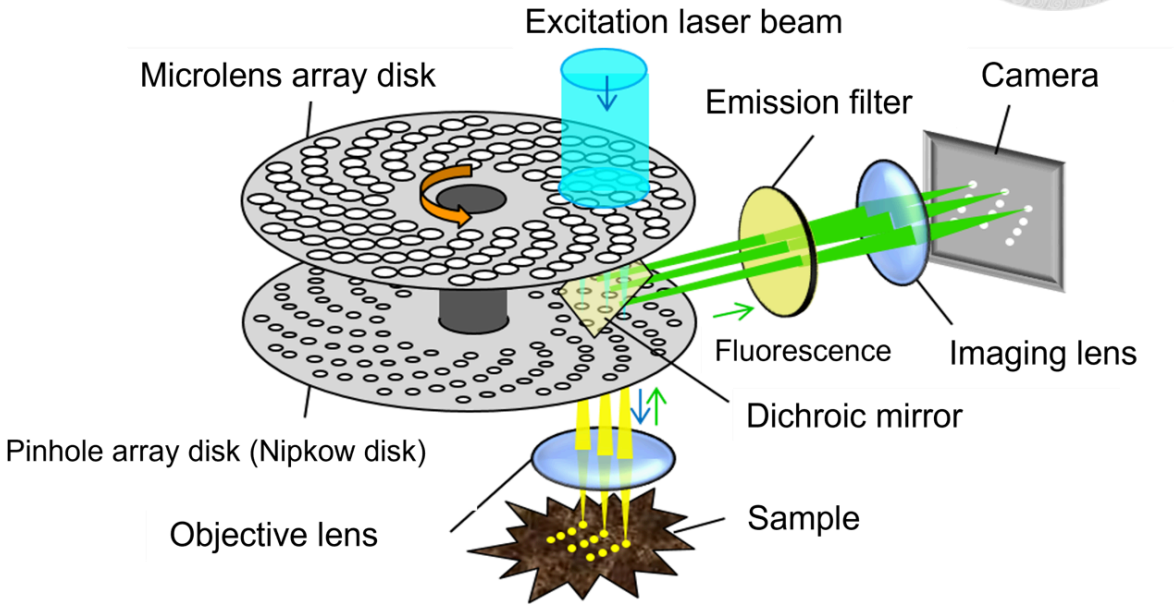

Figure 8: Illustration of optical path of Yokogawa spinning disk system. The figure is reproduced with permission from Yokogawa company.

doi:10.6342/NTU202400835

Ch3. Method

3.1 Optical system

Figure 9 depicts the optical setup of our multiphoton spinning disk system. The light source originates from a commercial Yb laser pump and optical parametric amplifier (OPA) system, specifically the Light Conversion CB3-40W and I-OPA model. The CB3-40W is capable of generating 1030 nm wavelength femtosecond laser pulses with a repetition rate of 1 MHz and an output power of 40 W, providing pulse energies of up to 40 μJ. It features a built-in pulse picker that allows us to control the output repetition rate from 1 kHz to 1 MHz. Additionally, there is a built-in attenuator comprising a half wave plate and polarized beam splitter, enabling us to decrease the pulse energy of each pulse. The OPA system further extends the spectrum to 640 – 1010 nm (Signal) and 1050 – 2600 nm (Idler), with maximum powers of around 1.5 W at 940 nm and 1 W at 1300 nm (1 MHz repetition rate).

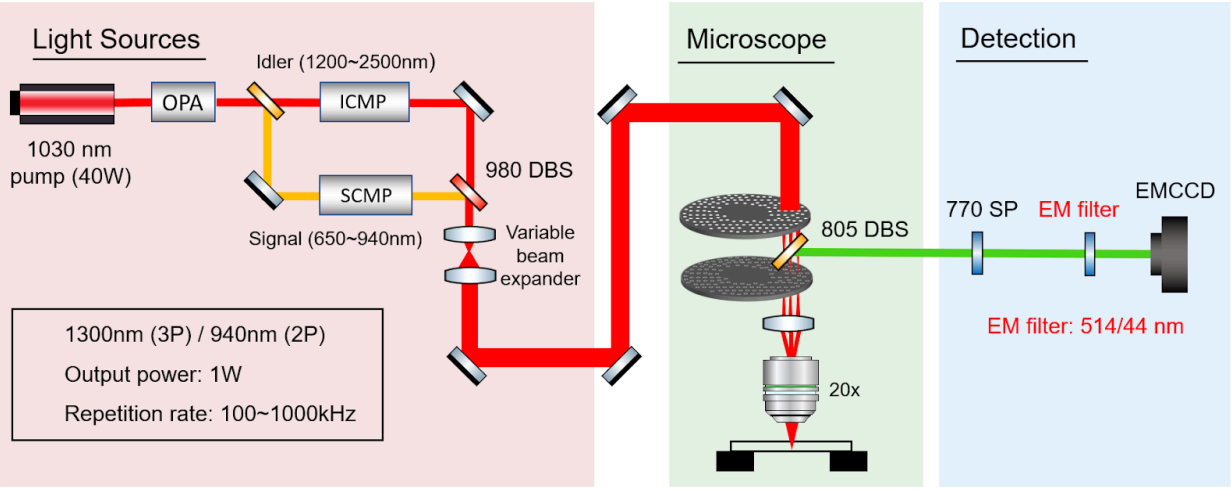

Figure 9: Optical setup of 3P spinning disk system. Where OPA stand for optical parametric amplifier, SCMP stand for compressor for signal, ICMP stand for compressor for idler, DBS stand for dicroic beam splitter and SP means short pass filter.

doi:10.6342/NTU202400835

The Compressor for Signal (SCMP) and Idler (ICMP) provide positive and negative dispersion, respectively, to compensate for the group delay dispersion (GDD) originating from the OPA system and compress the pulse. For example, according to the factory test report, the idler pulse at 1300nm after OPA is 102 fs and is reduced to 53.8 fs after passing through the compressor.

After passing through the compressor, we utilize a 980 long-pass dichroic to combine the signal and idler into the same beam path. Another 980 long-pass filter is placed inside the beam path while using the idler beam to further filter out the leaked signal spectrum within the idler beam. The beam then passes through the variable beam expander, ThorLabs ZBE2C - 1X - 4X Achromatic Zoom Beam Expander, which can expand the beam to cover the entire field of view. The tunability of the beam expander allows us to find the balance between the field of view and the excitation intensity of each sample.

Subsequently, the beam is introduced into the MP-spinning disk unit and passes through the Zeiss 20X NA 1.0 objective (W Plan-Apochromat 20x/1.0 DIC VIS-IR) , focusing on the specimen. The fluorescence signal is then collected by the objective, passes through the pinhole disk, and is reflected by the 805 dichroic beam splitter. It then traverses the 770 short-pass filter and a 514/44 emission filter before being collected by the EMCCD camera. We have two camera condensers, 1.2X and 2X magnification, allowing us to select suitable digital resolution and field of view (for the 20X objective, the pixel width is 0.645 μm for the 1.2X condenser and 0.332 μm for the 2X condenser). In the following experiment, all of the images are taken under 2X condenser except imaging of microfluidic chips in section 4.2. We utilized the software "SlideBook" to control the microscope and acquire data. This software is provided by 3i -

doi:10.6342/NTU202400835

Intelligent Imaging Innovations company, enabling us to seamlessly integrate and control the microscope, MP-spinning disk unit, and the EMCCD camera.

3.2 Selection of MP-spinning disk unit

The commercial spinning disk unit market is largely dominated by Yokogawa Electric Corporation, primarily due to their ownership of the dual-disk patent. Their flagship model, the Yokogawa Confocal Scanning Unit X1 (CSU-X1), is specifically designed for single-photon excitation. It boasts approximately 20,000 microlenses with a 250 μm diameter, and the corresponding pinholes have a 250-μm pitch and a 50 μm diameter. With a spinning speed of up to 10,000 rpm, each rotation can generate 12 complete images, resulting in a theoretical maximum frame rate of 2000 fps.

Given the inefficiency of multi-photon absorption compared to single-photon absorption, our multi-photon spinning disk system adopts a Multi-Photon version (CSU-MP) (Shimozawa et al., 2013). This version increases the microlens diameter and corresponding pinhole pitch to 580 μm with 100 μm pinhole diameter, increasing the excitation intensity of each focus. The total laser transmission also improves from 19.3% to 58.0% at 950 nm (Shimozawa et al., 2013), while the transmission at 1300 nm is approximately 36% based on our measurements. Despite maintaining the same spinning speed of up to 10,000 rpm, the the10oretical maximum frame rate decreases to 333 fps as each rotation can now only generate 2 complete images.

doi:10.6342/NTU202400835

3.3 Selection of the camera

Cameras serve as interfaces converting analog signals to digital information through the photoelectric effect. In modern camera-based fluorescence microscopy imaging, EMCCD (Electron Multiplying Charged Coupled Device) and sCMOS (scientific Complementary Metal–Oxide–Semiconductor) stand as two leading scientific imaging technologies, each offering distinct advantages in different situations. Over the past few decades, it has become evident that sCMOS holds a distinct performance advantage across most parameters, particularly in terms of speed, dynamic range, and resolution (pixel size). However, in extreme low-light applications, EMCCD technology still retains its advantage over sCMOS due to its higher quantum efficiency (State-of-the-art EMCCD ~95%, sCMOS ~65%) and lower readout noise.

The figure below, sourced from Andor, a leading company in EMCCD and sCMOS technologies, depict the signal-to-noise ratio across a range of light intensities for their best EMCCD iXon series and sCMOS Zyla series. These figures illustrate that EMCCD exhibits better SNR below 20 photons per pixel.

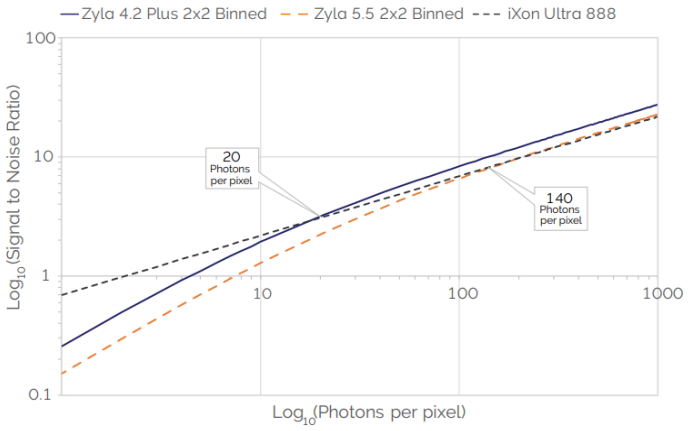

Figure 10: Comparison of signal-to-noise ratio across a range of light intensities of Top EMCCD and sCMOS. The figure is reproduced with permission from Andor company.

doi:10.6342/NTU202400835

Due to the weak signal of our three-photon spinning disk imaging, we employ the Andor iXon Ultra 888 EMCCD camera. The camera features active pixels of 1024 x 1024 with a pixel size of 13μm × 13μm, and its maximum quantum efficiency exceeds 95%.

CCD-based detectors, including EMCCD, utilize a silicon diode photosensor (pixel) connected to a charge storage region, which in turn links to a readout region, multiplication register (for EMCCD), and a read-out amplifier. The charge transfer and readout occur pixel by pixel, introducing a time limitation due to relatively slow readout speeds compared to CMOS (and sCMOS) technology. The frame rate of the iXon Ultra 888 represents the physical limit of our system, as shown in the chart below:

Binning \ Pixels	1024 x 1024	512x 512	256 x 256
1×1	26 Hz	50 Hz	95 Hz
2×2	50 Hz	94 Hz	170 Hz
4×4	92 Hz	167 Hz	281 Hz

Table 4: The frame rate of iXon Ultra 888 EMCCD camera under different conditions, the data is provided by Andor .

doi:10.6342/NTU202400835

3.4 Optimization of the 3P signal

For multiphoton excitation, it is necessary to use high-peak-power femtosecond pulse lasers to excite specimens. Because of the short pulse width, these pulses contain a broad range of wavelengths. As the pulse propagates through the optical elements, microscope, and objective, the pulse width broadens due to group delay dispersion (GDD), where each wavelength propagates at a different velocity in the material due to the dispersion relation. Typically, the GDD is positive in optical elements when the pulse wavelength is below 1500 nm.

As mentioned in section 3.1, the idler compressor (ICMP) provides positive dispersion to compensate for the negative dispersion of the idler generated from the OPA, ensuring it has the narrowest pulse after the compressor. However, when the laser pulse passes through our system's lenses, filters, and objective, the positive dispersion of each element will expand the pulse again. The dispersion of the ICMP and optical elements are on the same side. Hence, to mitigate the effect of the positive dispersion in our system, we remove the ICMP during experiments to increase the fluorescent signal.

Another way to further increase the 3P signal is to shrink the excitation beam. We have tested this method by replacing the variable beam expander with a 4f system composed of two plano-convex lenses whose focus lengths are 150.0 mm (Thorlab LA1433-C) and 75.0 mm (Thorlab LA1608-C) respectively. This adjustment increases the intensity of each focus at the expense of sacrificing the illumination field of view. Below the figure 11 shows the effect of removing ICMP and shrinking the excitation beam.

doi:10.6342/NTU202400835

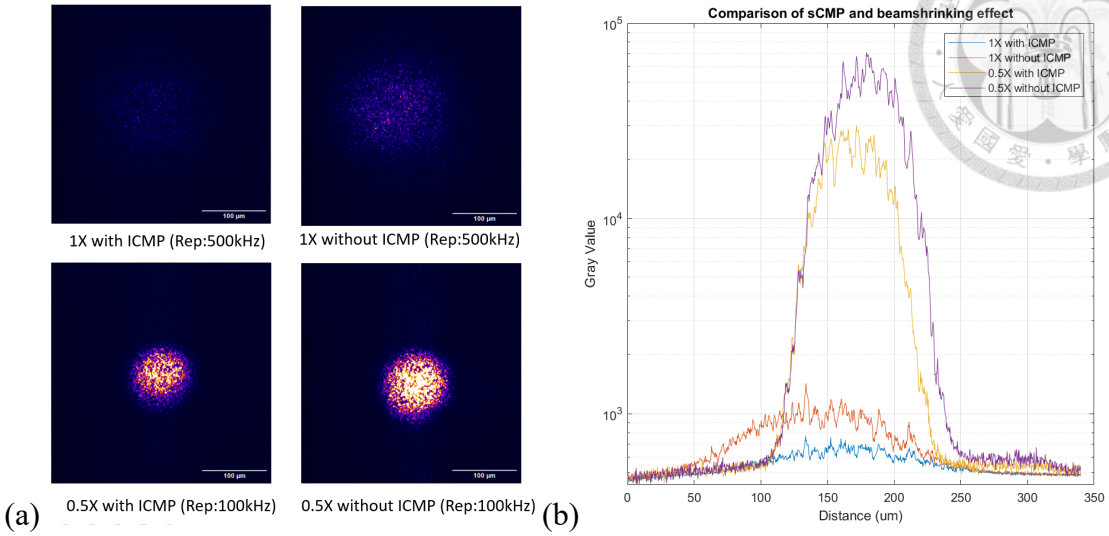

Figure 11: the comparison of the effect of removing ICMP and shrinking the excitation beam. (a) The images of dense 1 μm green fluorescent beads under 4 different conditions: 1X (original beam size, without beam eabander) with ICMP, 1X without ICMP, 0.5X (shrinking beam through 4f system) with ICMP, and 0.5X without ICMP.The repetition rate of 0.5X image (100kHz) is lower than 1X image (500kHz) to prevent photobleaching of the sample. (b) We select a 1024*150 pixels ROI (x*y) across the center of the illumination area in each image and plot the intensity profile versus the x-axis in the semilog scale. The intensity profile of 0.5X is already multiplied by 5 to compensate for the difference of laser repetition rate.

Figure 11 shows the images of a dense 1 μm green fluorescent beads sample (Invitrogen™ FluoSpheres™ Carboxylate-Modified Microspheres F8823, consisting of 1 μm green fluorescence beads with excitation and emission wavelengths at 505/515 nm) which is acquired by different configuration, including with/without ICMP and with/without shrinking excitation beam, respectively. The laser built-in attenuator is set at the same step (88%) for each image hence the pulse energy of each image is at a similar level. The repetition rate of 1X (original beam size) is set at 500 kHz while is set at 100 kHz for 0.5X (shrinking beam through 4f system) condition. The average excitation power after the objective of 1X condition with and without

doi:10.6342/NTU202400835

ICMP is 47.4 mW and 50.4 mW respectively, and 0.5X condition with and without ICMP is 8.175 mW and 8.375 mW respectively.

According to the results in figure 11(b), we find that the signal enhancement of removing ICMP is around 2 times and the effect of shrinking the excitation beam enhances the signal by more than 50 times. Note that 1X and 0.5X images were images at the same sample but in different regions.

In the following experiment, however, to achieve suitable FOV and compared with 2P imaging, we didn't apply beam shrinking 4f system nor variable beam expander in the optical system.

3.5 Calculation of attenuation length

To quantify the excitation penetration in biological tissue, the attenuation length (l_a) is widely employed. The attenuation length is defined as the distance at which the intensity of the excitation beam drops to 1/e inside the tissue, which can be mathematically expressed as:

$$I(d) = I_0 e^{-d/l_a} = I_0 e^{-\mu_{att} \times d}$$

Where I(d) is the excitation intensity at depth d, I_0 is the intensity at the surface and μ_{att} is attenuation coefficient which is the inverse of l_a. In multiphoton excitation (MPE) processes, the n-th order multiphoton fluorescence intensity $F^{(n)}(d)$ is related to the excitation intensity I(d) by the following equation:

$$F^{(n)}(d) \propto (I(d))^n$$

Hence, fluorescence intensity is a function of the attenuation length:

doi:10.6342/NTU202400835

$$F^{(n)}(d) = a \times e^{-nd/l_a}$$

Taking the natural logarithm of both sides of the equation, we can derive:

$$\ln\left(F^{(n)}(d)\right) = \ln(a) - \frac{n \times d}{l_a}$$

Equation above shows the relation between fluorescence intensity decays with depth. By plotting the dependence of $\ln\left(F^{(n)}(d)\right)$ on d, the slope is -n/l_a, consequently we can derive l_a = (-n/ slope).

doi:10.6342/NTU202400835

Ch4. Experiments and Results

4.1 3P power dependent test

To evaluate the power-dependent behavior of three-photon fluorescence, we employ Invitrogen™ FluoSpheres™ Carboxylate-Modified Microspheres F8823, consisting of 1 μm green fluorescence beads with excitation and emission wavelengths at 505/515 nm, depositing the fluorescence bead solution directly onto a glass slide to create a dense 2D fluorescence bead sample. Subsequently, we capture three-photon images without using a beam expander, setting the laser pulse repetition rate at 500 kHz, while adjusting the pulse energy by laser built-in attenuator from step 88% to step 100%. The exposure time is 240 ms for each image, and maintaining all other parameters constant.

The procedure commences with lower power settings, gradually increasing the power and capturing images at each step. Since we utilize high power for three-photon excitation, to ensure the emission intensity is not affected by photobleaching, we then decrease the power to take the image at the same excitation intensity to ensure the trend is similar at increasing and decreasing intensity.

Figure 12(a) illustrates the image of the green fluorescent bead, with the yellow circle frame indicating the Region of Interest (ROI) for intensity analysis. We utilized the average intensity within the ROI as the signal, and the results are depicted in Figure 12(b).

doi:10.6342/NTU202400835

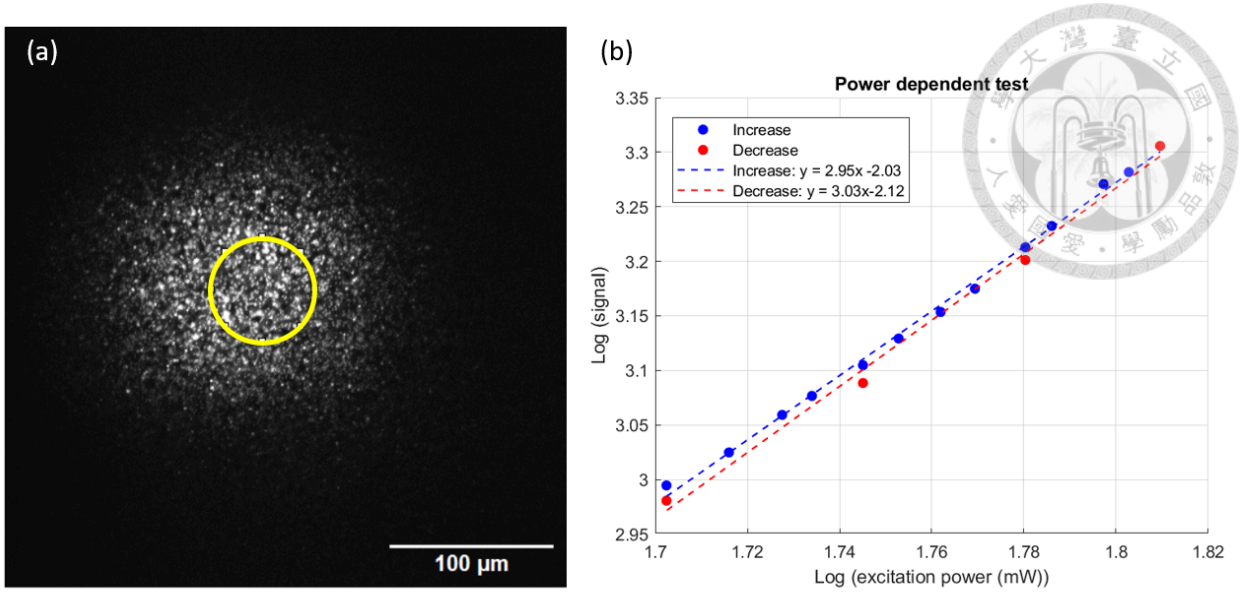

Figure 12: 3P power-dependent measurement of 1μm fluorescent bead (the imaging is acquire without ICMP and beam expander).(a) Image of a green fluorescent bead with the yellow circle indicating the ROI selected for power-dependent analysis.(b) Log-log plot illustrating the relationship between excitation power and fluorescence signal intensity. Blue dots represent measurements taken during increasing excitation intensity, while red dots represent measurements during decreasing excitation intensity.

In Figure 12(b), which represents the log-log plot of excitation power and signal intensity, we observed that the power-dependent trend of increasing intensity (denoted by gray) closely mirrored the trend during decreasing intensity, indicating small impact from photobleaching. The slope of the log-log plot for power dependence was measured as 2.95 ± 0.089 (during increasing intensity) and 3.03 ± 0.38 (during decreasing intensity), respectively, consistent with the characteristics of three-photon absorption.

doi:10.6342/NTU202400835

4.2 Demonstrate the speed: microfluidic chip

To demonstrate our system's speed capabilities, we simulated a blood vessel using a custom microfluidic chip featuring three microtubes, each with a 100 μm diameter, on a PDMS substrate covered by a 0.15 mm glass cover. These microtubes are interconnected with two holes on the chip's other side, allowing for the insertion of flexible hoses connected to syringes for controlled fluid injection. In our experiments, we utilized a solution containing 10 μm green fluorescence beads (Invitrogen F8836), similar to typical red blood cells (6 ~ 8 μm in diameter), imaged by our three-photon spinning disk system. The laser repetition rate was set at 500 kHz, with the laser's built-in attenuator at 100%, yielding an average power of 95.25 mW, and an exposure time of 3 ms per frame.

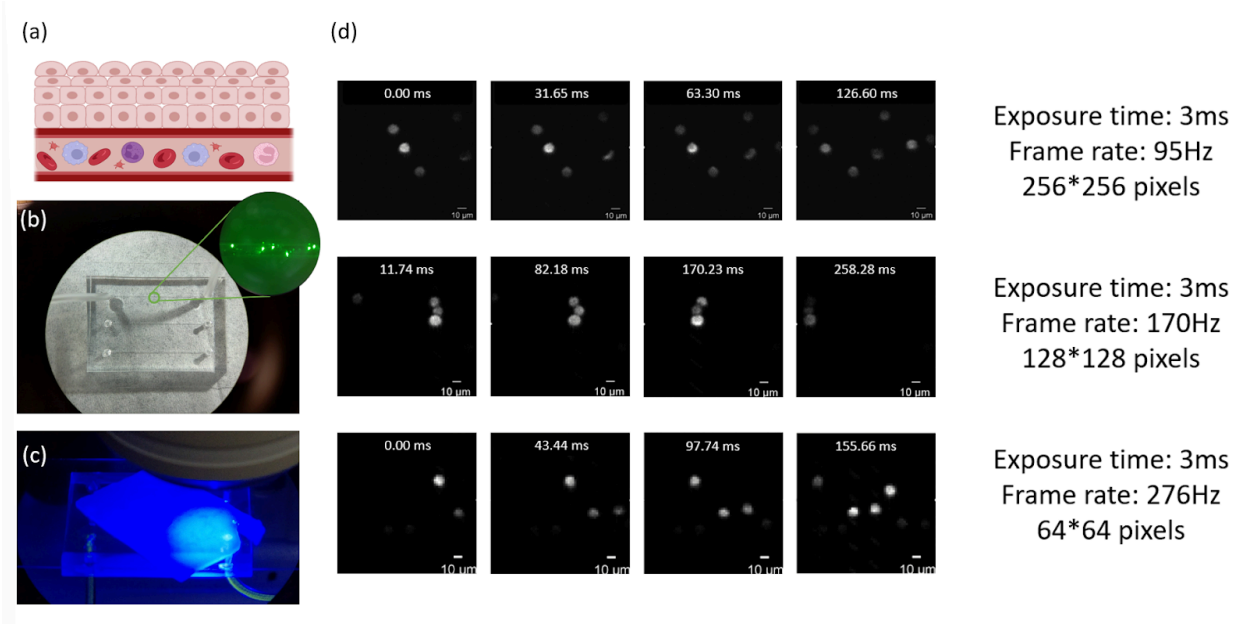

Figure 13: Imaging of flowing fluorescent beads under pseudo-scattering tissue. (a) Illustration of blood vessel inside tissue. (b) Microfluidic chip system setup (100 μm diameter). (c) Pseudo-scattering tissue on microfluidic chip under blue-LED illumination. (d) 3P time-series imaging of floating fluorescent beads at different frame rate under different camera settings. The bellowed link is the video with 276 Hz frame rate: https://drive.google.com/file/d/18eGHjOaKTZ6aKezPAS-jJFUZpfCKelOG/view

doi:10.6342/NTU202400835

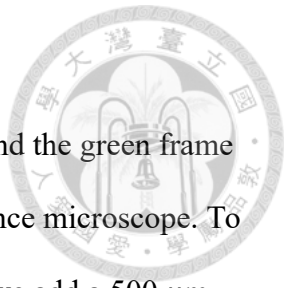

Figure 13b shows the microfluidic chip under the dissecting microscope, and the green frame shows the fluorescent bead inside the microfluidic chip under the fluorescence microscope. To further demonstrate the ability of imaging under a scattering environment, we add a 500 μm thick pseudo scattering tissue made from 5% fresh milk inside 1% agarose solution as Figure13b shows.

Our spinning disk system has a minimum acquisition time of 3 ms, as discussed in Chapter 3. The actual speed limit of our system is the EMCCD camera as pointed out by Table 3 in Chapter 3.3. Note that the achieved frame rates may slightly differ from those listed in Table 3 due to the limitation of exposure time in our system, which is set at 3 ms. Figure 13c shows the sequential images captured under a 3 ms exposure time, with frame rates of 95 Hz at 256*256 pixels, 170 Hz at 128*128 pixels, and 276 Hz at 64*64 pixels, respectively.

4.3 Attenuation length measurement — fixed mouse brain

To further demonstrate the capabilities of our imaging system as well as the comparison of attenuation length of 2P and 3P imaging of the spinning disk system, we perform experiments on fixed mouse brains. The mouse brain was labeled with Thy1-eGFP, a common fluorescent marker used in neuroscience research. The mouse was perfused with phosphate buffered saline and followed withed 4% paraformaldehyse. The brain tissue was sliced vertically with a thickness of 2000 μm, and no additional tissue cleaning processes were performed to maintain its

doi:10.6342/NTU202400835

natural state. However, after fixing, the scattering becomes stronger compared to *in vivo* mouse brains, where scattering lengths in *in vivo* mouse brain samples are around 2 ~ 3 times higher than fixed samples (Imperato et al., 2022).

To evaluate the attenuation characteristics of both two-photon excitation (at 940 nm) and three-photon excitation (at 1300 nm), we selected regions of the brain where neuron somas are dense and more evenly distributed (Figure 14).

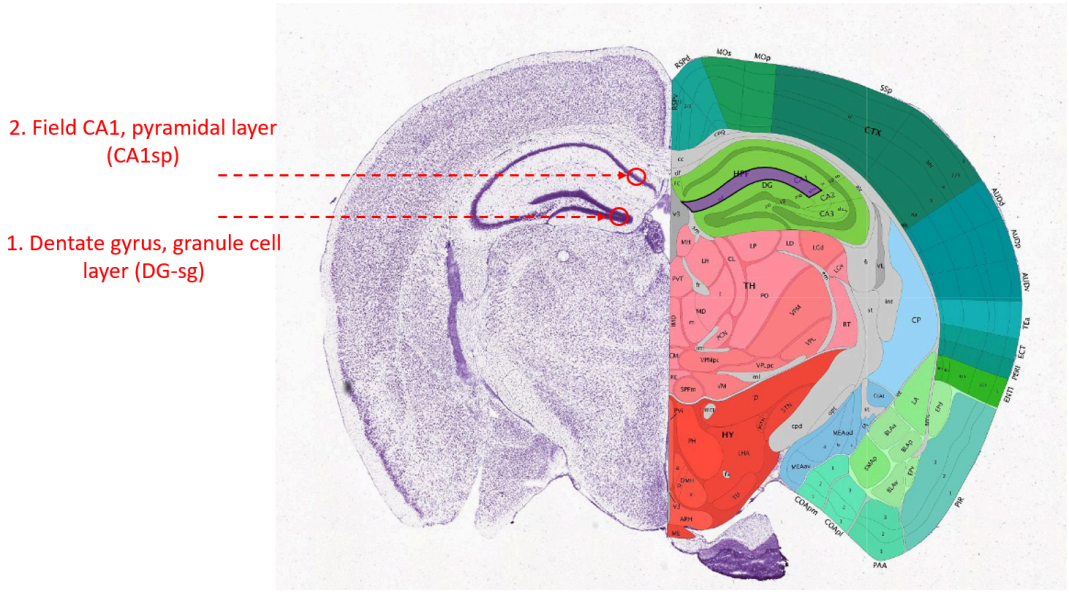

Figure 14: The mouse brain regions we selected for imaging. Nissl (left) and anatomical annotations (right) from the Allen Mouse Brain Atlas – Adult Mouse Brain, https://atlas.brain-map.org/.

Subsequently, we acquired z-stack images using both two-photon and three-photon excitations, allowing us to analyze the fluorescence signal at various depths within the tissue. By comparing the fluorescence intensity profiles obtained from the z-stack images acquired with both excitation wavelengths (940 nm and 1300 nm), we derive the attenuation lengths associated with each

doi:10.6342/NTU202400835

wavelength. This analysis provides insights into the depth penetration capabilities of our imaging system under different excitation conditions and wavelengths.

Figures 15a and 15b depict the x-y and x-z views, respectively, of the two-photon (2P) image captured from Dentate gyrus, granule cell layer (DG-sg) of the fixed mouse brain slice where neuron somas are densely distributed. Conversely, Figure 15c and 15d showcase the x-y and x-z views of the three-photon (3P) image obtained from the same region.

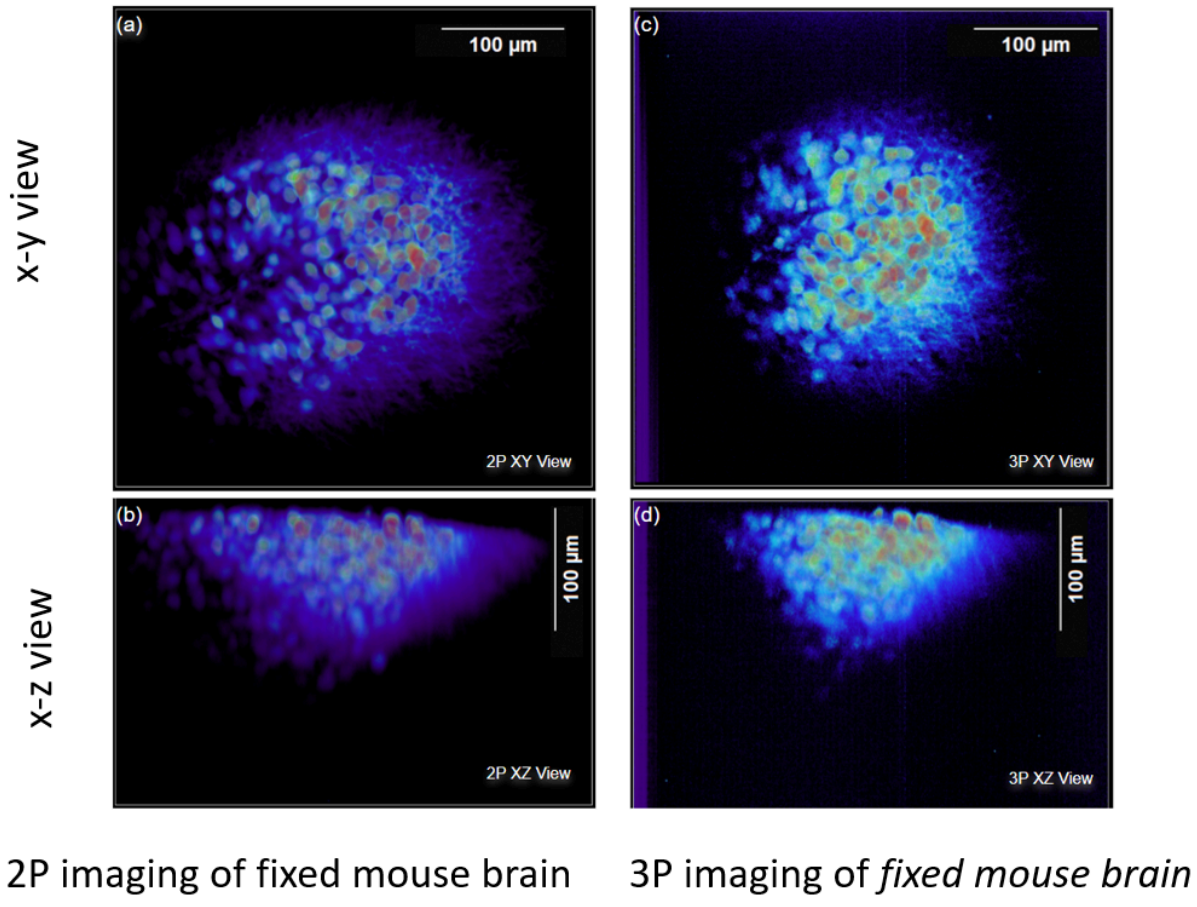

Figure 15: Imaging of fixed mouse brain (a) x-y view of 2P imaging (b) x-z view of 2P imaging (c) x-y view of 3P imaging (d) x-z view of 3P imaging

doi:10.6342/NTU202400835

In this experiment, the repetition rate of 2P excitation is set at 100 kHz with average power 19.04 mW after objective; the 3P excitation is set at 1 MHz repetition rate with average power 190.5 mW after objective. The exposure time of each frame is 240 ms with 2x2 binning, the step size of z is 1 μm.

To conduct a quantitative comparison of the attenuation lengths associated with two-photon and three-photon wavelengths, we adopt a methodology similar to that outlined in (Horton et al., 2013; Hsu et al., 2019; Kobat et al., 2009). Initially, we designate a region of interest (ROI) measuring 100 μm * 100 μm, delineated by the red rectangle frame visible in Figure 16(a)(b). Subsequently, we compute the signal intensity for each layer by averaging the pixel values of the top 5% within the selected ROI.

The results are presented in Figure 16(c), where the blue and orange dots correspond to the signal intensities for two-photon and three-photon excitation, respectively, in each layer. Additionally, the blue and orange dashed lines represent the linear regression lines fitted to the respective datasets.

doi:10.6342/NTU202400835

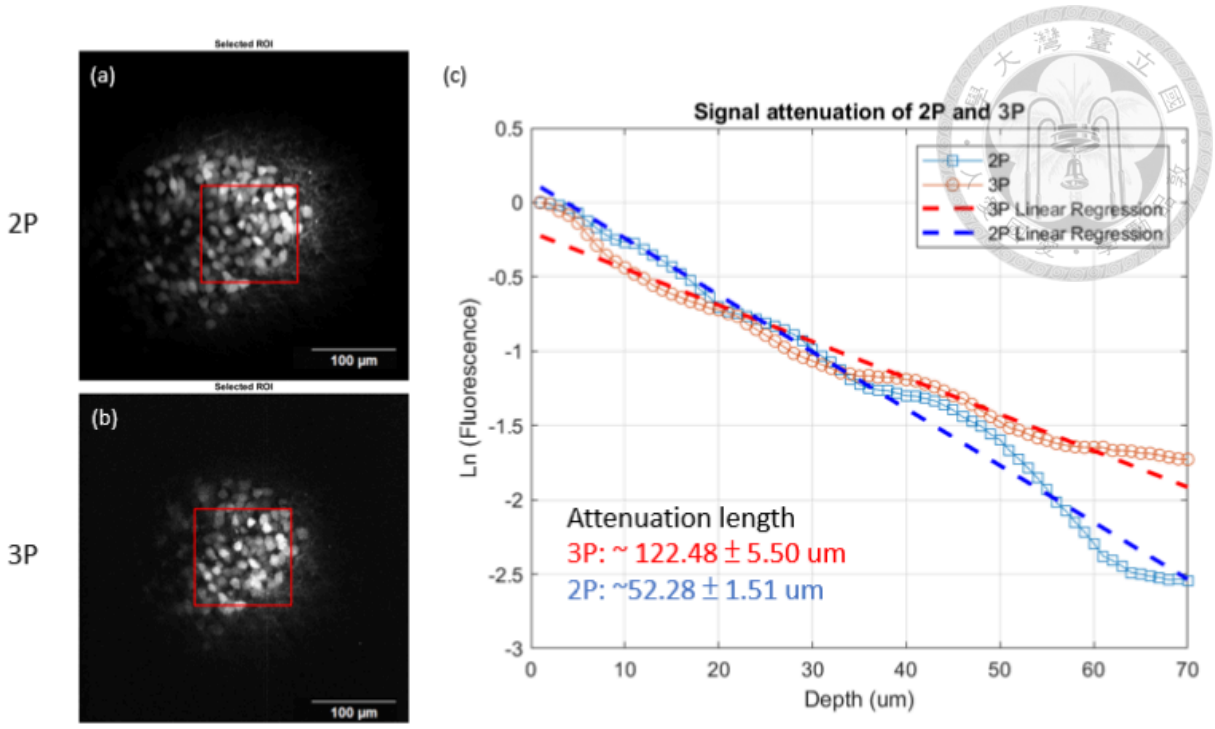

Figure 16: Analysis of signal attenuation of fixed mouse brain. (a) x-y view of 2P imaging (b) x-y view of 3P imaging.(c) the signal attenuation of 2P and 3P imaging

From our analysis, we find out that the attenuation length for 3P excitation is approximately 122 μm, while for 2P excitation, it is about 52 μm within this image stack. Where the attenuation length ratio between 3P and 2P is around 2.3 times.

It's important to emphasize that the attenuation length can vary in tissue properties (Wang et al., 2018). Consequently, these values and ratios between 3P/2P may differ across various samples and even within different regions of the same specimen (Wang et al., 2017). Hence, we also conduct another imaging analysis focusing on the Field CA1, pyramidal layer (CA1sp) of the fixed mouse brain slice.

doi:10.6342/NTU202400835

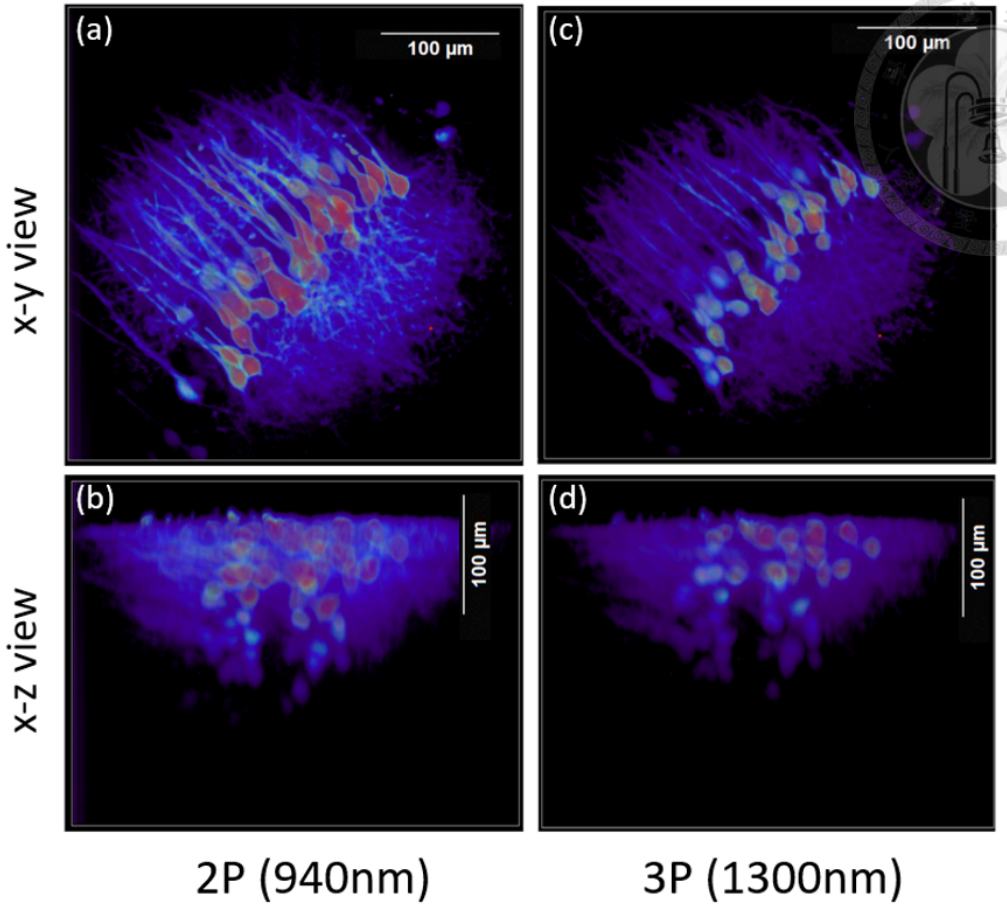

Figure 17: Imaging of fixed mouse brain (a) x-y view of 2P imaging (b) x-z view of 2P imaging (c) x-y view of 3P imaging (d) x-z view of 3P imaging .

Figure 17 depicts the region of CA1 pyramidal layer (CA1sp) of the fixed mouse brain, showcasing the soma and dendrites of pyramid cells. In this image set, the repetition rate of 2P excitation is set at 100kHz with average power 19.04 mW after objective; the 3P excitation is set at 1 MHz repetition rate with average power 190.4 mW after objective. The exposure time of each frame is 240 ms with no binning for 2P imaging and 2x2 binning for 3P imaging, the step size of z is 1 um.

doi:10.6342/NTU202400835

Following a methodology similar to our previous analysis, we selected a 100 μm × 100 μm region of interest (ROI) at the center of the image (Figure 18(a)(b)). We then computed the average intensity of the top 5% brightest pixels within this ROI, layer by layer, to derive the signal attenuation length (Figure 18 (c)).

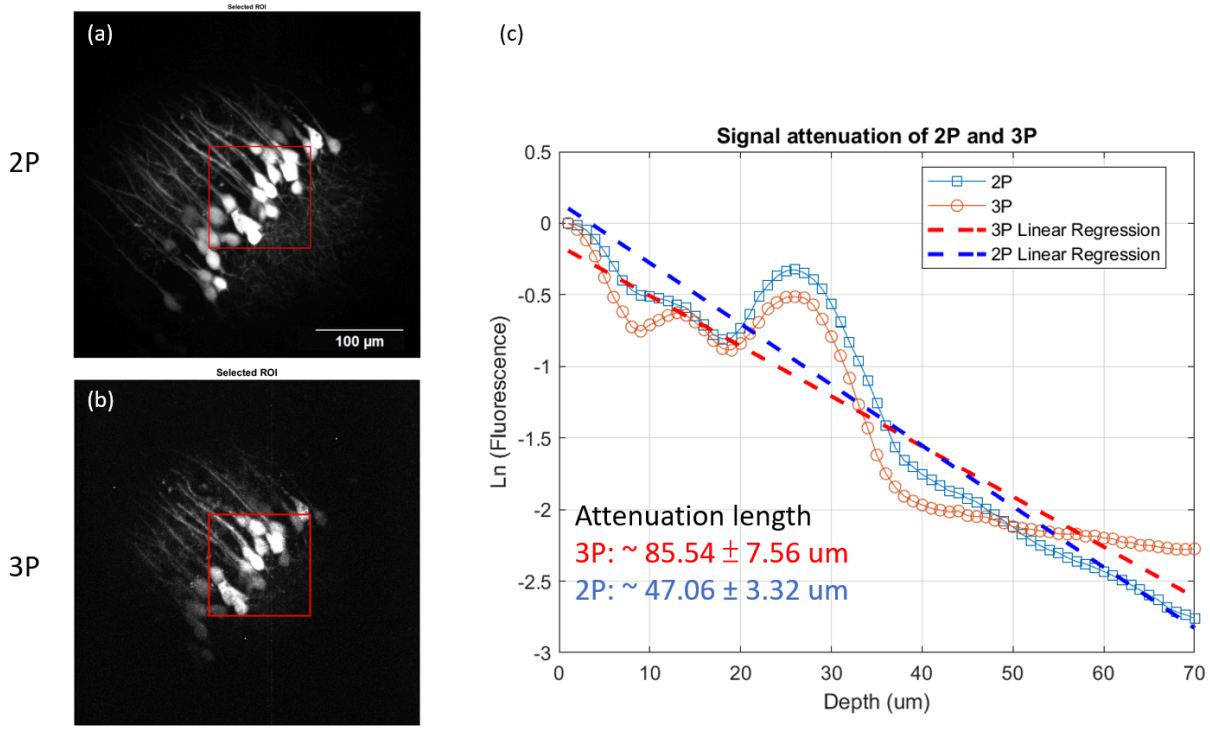

Figure 18: Analysis of signal attenuation of fixed mouse brain. (a) x-y view of 2P imaging (b) x-y view of 3P imaging.(c) the signal attenuation of 2P and 3P imaging.

Compared to Figure 16(c), here the signal variation across the axial direction is much more deviated from a linear trend. The possible reason is the co-existence of some and dense fibers. In this specific region, we found that the attenuation length for 3P excitation is approximately 86 μm, while for 2P excitation, it is approximately 47 μm. In this region, both the 3P and 2P attenuation lengths are shorter compared to those observed in the previous sample. The ratio between the attenuation lengths of 3P and 2P excitation is approximately 1.8 times.

doi:10.6342/NTU202400835

4.4 Attenuation length measurement — *in vivo Drosophila* brain

In addition to imaging fixed mouse brain samples, we also demonstrate the capabilities of our system with *in vivo Drosophila*, a widely utilized animal model in neuroscience research. The *Drosophila* sample we utilized is genetically engineered with the gene type: OK107-GAL4; UAS-GFP, which labels green fluorescent protein on the mushroom bodies of the *Drosophila* brain. Mushroom bodies are a pair of structures present in the brains of arthropods and play a pivotal role in olfactory learning and memory processes.

To conduct *in vivo* imaging, we first immobilize the living *Drosophil*a by freezing it and then fixing it onto a homemade mount with its head facing upwards and covered by saline solution. Subsequently, using fine tweezers, we perform microsurgery to carefully remove the head cuticle and underlying air sacs. Following this preparation, we utilize the spinning disk microscope to acquire images of the *Drosophila* brain *in vivo*.

Figure 19 presents the x-y and x-z views of both 2P and 3P imaging of the *in vivo Drosophila* brain.The repetition rate of 2P excitation is set at 33 kHz with average power 20.8 mW after objective; the 3P excitation is set at 1 MHz repetition rate with average power 190.4 mW after objective. The exposure time of each frame is 240 ms with no binning for both imaging, the step size of z is 1 μm.

doi:10.6342/NTU202400835

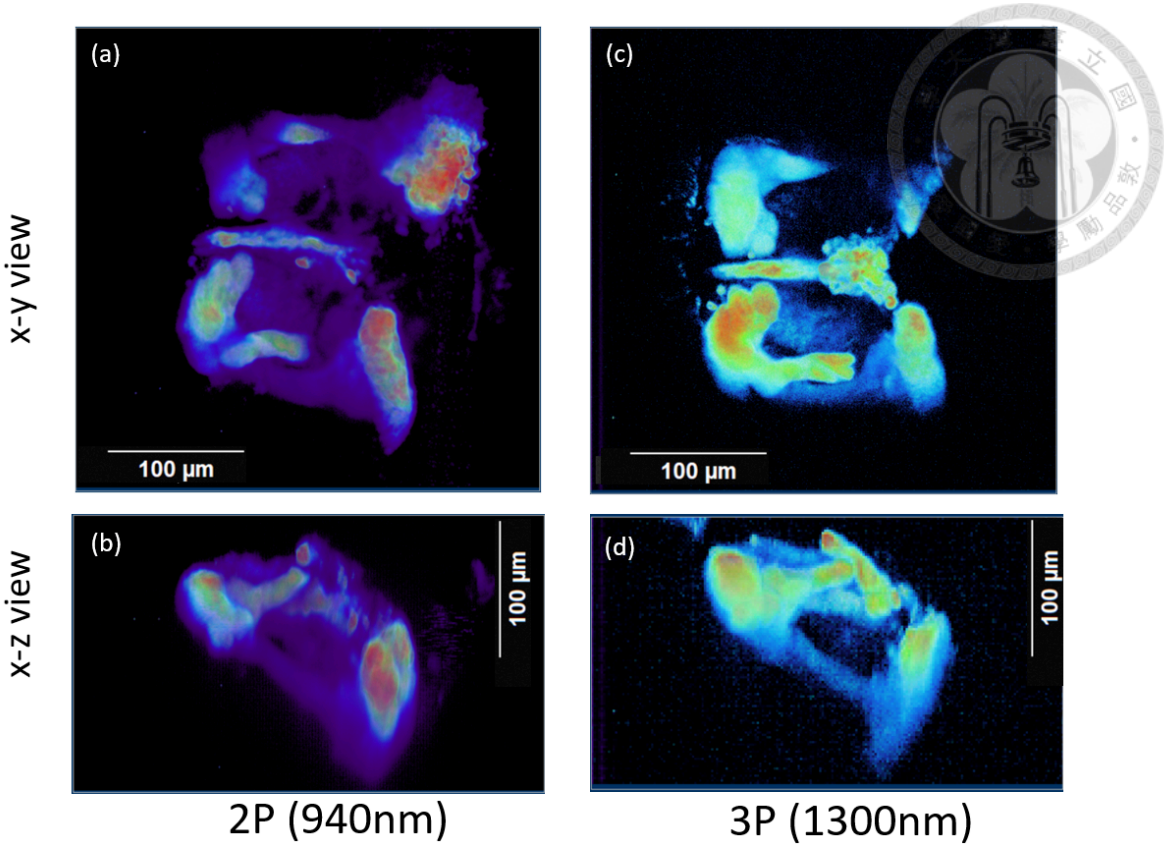

Figure 19: Imaging of *in vivo Drosophila* brain (a) x-y view of 2P imaging (b) x-z view of 2P imaging (c) x-y view of 3P imaging (d) x-z view of 3P imaging

In Figure 19, we can clearly observe the mushroom body structure in both the 2P and 3P images. The Drosophila's orientation is directed towards the left, hence Figures 19(a) and (c) exhibit vertically symmetrical structures. In Figures 19(a) and (c), the structures on the left side including the α/β, α'/β', and γ lobes, while the bright aggregates on the right are the soma of Kenyon cells.

To analyze the attenuation properties of 2P and 3P excitation quantitatively, we focus on the Kenyon cells region, where the structure is more evenly distributed. Figure 20 shows 4 sets of *Drosophila* Kenyon cells images umaging under 2P and 3P excitation. In each image set, the

doi:10.6342/NTU202400835

repetition rate of 2P excitation is set at 33kHz with average power 3.8 mW after objective; the 3P excitation is set at 1 MHz repetition rate with average power 125.2 mW after objective. The exposure time of 3P is 500ms each frame with 2x2 binning, and is 240 ms with no binning for 2P imaging, the step size of z is 1 μm.

doi:10.6342/NTU202400835

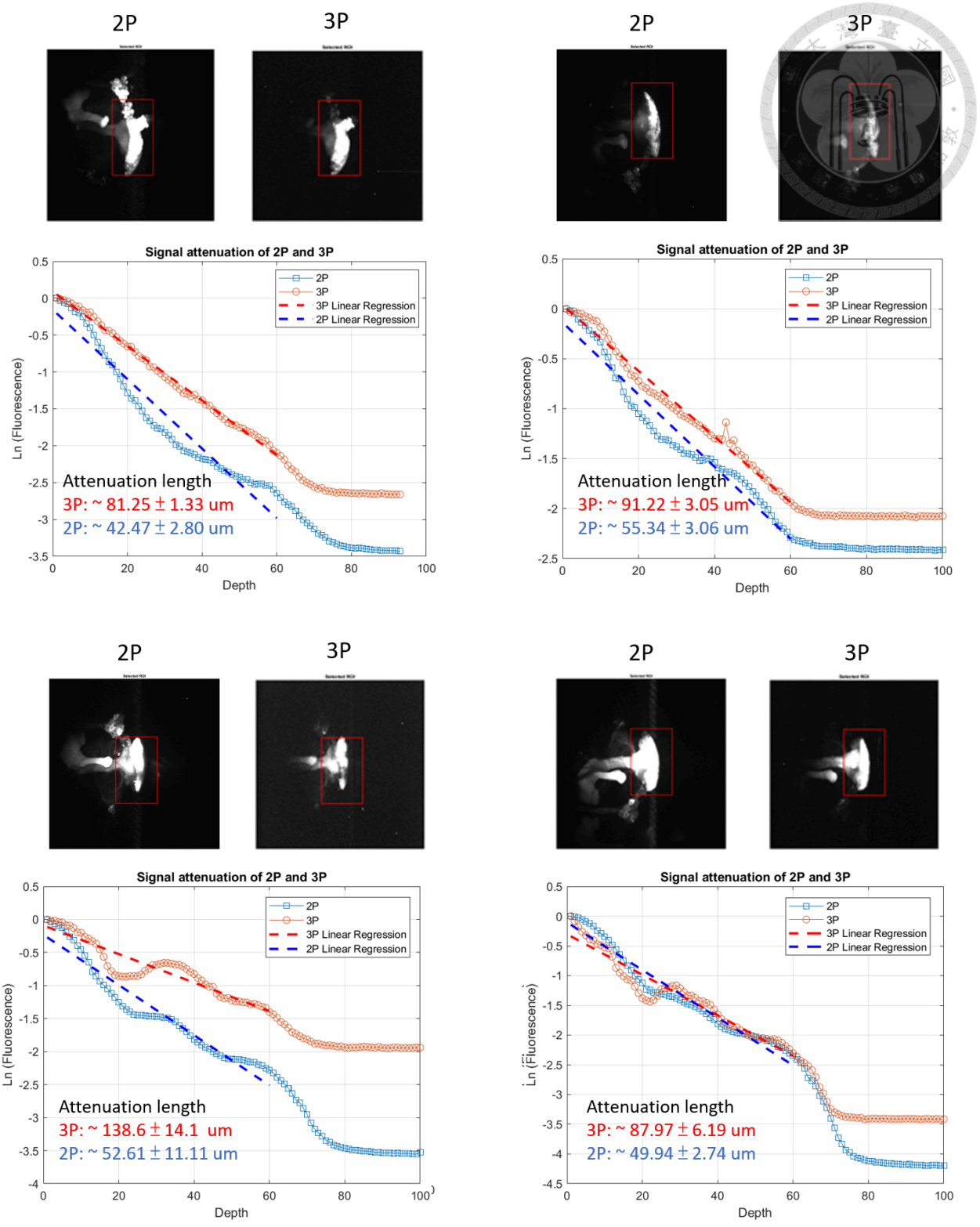

Figure 20: Attenuation length analysis of 3P and 2P attenuation length of 4 set of *Drosophila* Kenyon cells region

doi:10.6342/NTU202400835

According to the results, the attenuation length of 3P ranges from around 80 μm to 140 μm, while the attenuation length of 2P ranges from around 40 μm to 55 μm. The average ratio of 3P attenuation length to 2P attenuation length is around 2 times, which is similar to the results obtained from the fixed mouse brain.

To verify that the attenuation variation in Figure 20 is not due to systematic error, and to assess the repeatability of attenuation quantification, we analyzed the images taken under the same criteria in the same region during the experiment to assess the repeatability of the attenuation measurement. Figure 21 shows the 3P images of the *in vivo Drosophila* brain alpha and beta lobe region, with two image stacks taken under the same criteria. In the 3P-2 stack, a bright line is visible on the stack's surface, potentially resulting from tissue burning and causing a camera error. Therefore, during the experiment, we maintained consistent imaging criteria and imaging the same region twice.

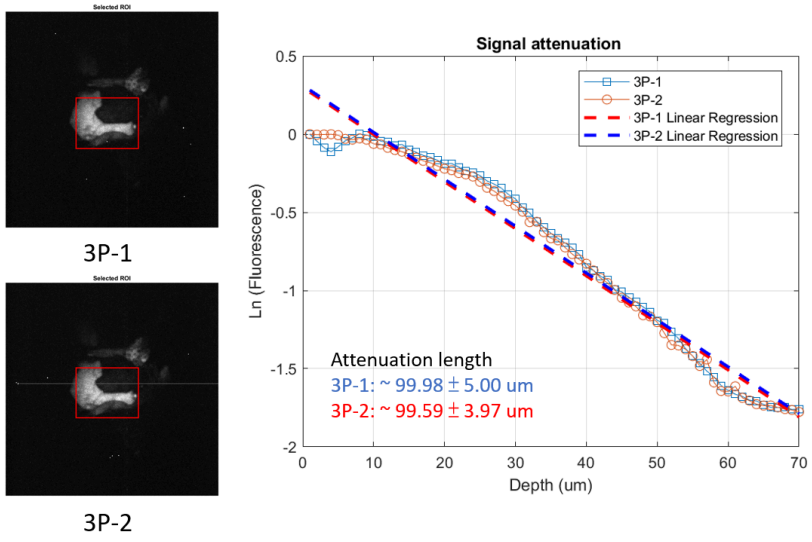

Figure 21: Repeated test of attenuation length measurement

doi:10.6342/NTU202400835

According to the results, the signal attenuation of the two image sets is almost identical, with attenuation lengths of 99.98 μm and 99.59 μm, respectively, demonstrating the repeatability of the experiment.

4.5. Discussion

In Section 4.1 we demonstrate the ability of capturing fluorescent signal a 3 ms exposure time, with frame rates of 95 Hz at 256*256 pixels, 170 Hz at 128*128 pixels, and 276 Hz at 64*64 pixels, respectively, by our spinning disk system. Below images reproduced from (Wu et al., 2021) shows the speed scaling comparison of highs-speed 2P (grey dot), 3P (red dot) (Ouzounov et al., 2017; Rowlands et al., 2017; Weisenburger et al., 2019) and our 3P spinning disk microscopy.

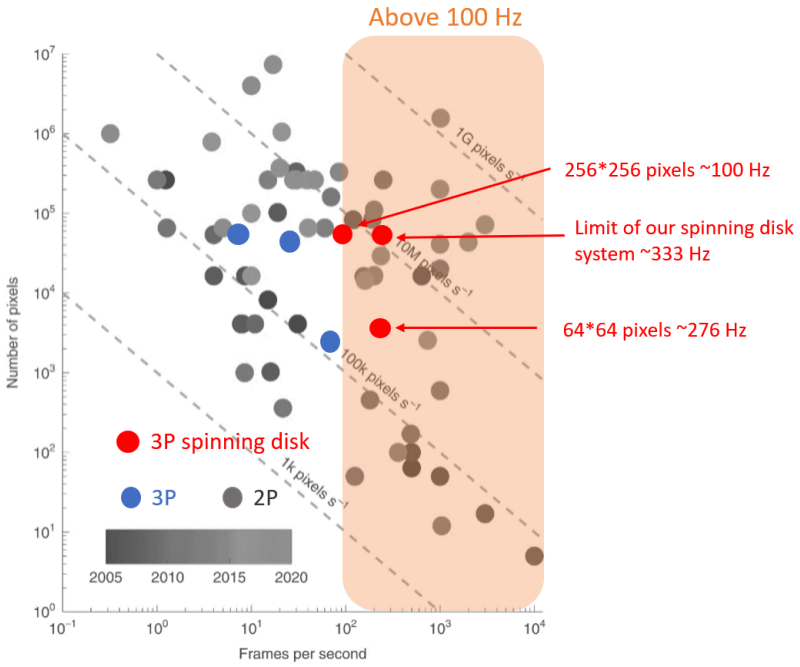

Figure 22: The speed scaling comparison of high-speed 2P (grey dots), 3P (blue dots), and our 3P spinning disk microscopy (red dots). The orange part in the figure indicates the region where the frame rate exceeds 100 Hz. The figure is reproduced with permission from (Wu et al., 2021).

doi:10.6342/NTU202400835

The results demonstrate the ability of our system to perform 3P images beyond 100 Hz frame rate, which is currently the fastest 3P imaging system.

In Section 4.3 and 4.4, we imaged and measured the attenuation length of fixed mouse brain and *in vivo Drosophila* brain. In fixed mouse brain, the attenuation length for 3P excitation is roughly twice that of 2P excitation in these experiments, consistent with previous findings in mouse brain cortex studies by 3P and 2P point scanning microscopy (Wang et al., 2020). This indicates that the 3P and 2P spinning disk microscope have the similar characteristic compared with point scanning microscopy in the aspect of improving penetration depth. Both of the 2P and 3P attenuation lengths in our study are notably shorter than those reported for *in vivo* mouse brain imaging. This discrepancy can be attributed to the increased scattering introduced during the tissue fixation process (Imperato et al., 2022).

In our experiments, the average ratio of 3P attenuation length to 2P attenuation length is around 2 times in the Kenyon cell region of the *in vivo Drosophila* Brain, similar to the results obtained from the fixed mouse brain. It is worth noting that this ratio differs from the findings of a previous study by Hsu et al., who indicated that the attenuation length ratio between 3P and 2P is around 1.5 times in the *in vivo Drosophila* brain (Hsu et al., 2019). This difference may be attributed to the fact that we were measuring on different gene types of *Drosophila*, which label the green fluorescent protein on different structures, and imaged different regions of the *Drosophila* brain.

doi:10.6342/NTU202400835

Since one of the advantages of our system is to perform functional imaging, we have also attempted *in vivo* functional imaging on genetically encoded calcium indicator (gene type: GMR48B06-GAL4/Cyo ; GC6f/TM3) labeled *Drosophila* brain. However, the fluorescence signal of this indicator is much weaker than that of the OK107-GAL4 gene type, making it inefficient to image under three-photon excitation. One potential solution to this problem is to identify a brighter gene type, or alternatively, to further optimize the microscopy system. The latter option will be discussed in Chapter 5.2.

doi:10.6342/NTU202400835

Ch5. Conclusion and Outlooks

5.1 Conclusion

In this work, we customized a multi-photon spinning disc unit with a tunable high-power femtosecond laser to demonstrate the first three-photon spinning disk microscopy. We achieving ~300 Hz frame rate which is currently the highest frame rate 3P microscope. We demonstrate its applications on flowing green fluorescent beads in microfluidic chip, fixed mouse brain and *in vivo Drosophila* brain. Furthermore, similar to previous studies done by point scanning multiphoton microscope, our findings from brain tissue imaging reveal that three-photon spinning disk imaging exhibits a lower attenuation rate when compared to its two-photon spinning disk counterpart, indicating better performance in deep tissue imaging. Our research paving the way for utilizing three-photon spinning disk microscope on high-speed deep tissue imaging.

5.2 Outlooks

The primary bottleneck of the 3P spinning disk system lies in the insufficient pulse energy resulting from the inefficient 3P excitation process. In our research, we addressed this challenge by illuminating only a fraction of the field of view, significantly smaller than the spinning disk system's full capacity (approximately 1/16 without a beam expander).

doi:10.6342/NTU202400835

There are two suggestions to improve the signal in our 3P spinning disk microscope without altering the laser source. As discussed in section 2.1, the signal of multiphoton excitation can be enhanced by a factor of $(I)^n/(\tau R)^{n-1}$. Therefore, one approach is to minimize the pulse duration after the objective. Although we removed the ICMP in the commercial laser system to shorten the pulse duration at the specimen stage, it is still not optimized to the best condition.

To optimize it further, we can first utilize an Autocorrelator to measure the ultrafast pulse width and then employ a femtosecond pulse compressor to compensate for the group delay dispersion (GDD) generated by the optical elements during the beam passage. This optimization aims to minimize the pulse duration and, consequently, increase the fluorescence signal intensity.

Another method to enhance the fluorescence signal involves increasing the pulse energy of each pulse. As discussed in sections 2.2 and 3.2, a notable intensity decrease occurs as the beam passes through the spinning disk, accounting for approximately 63% decrease in our spinning disk system. Reducing such decrease could significantly enhance the fluorescent signal or allowing us to increase the excitation field of view.

One suggestion is to utilize diffractive optical elements (DOE) and design a suitable pattern to place on the rotational stage. As the stage rotates, the beamlet will scan through the field of view in a manner similar to the spinning disk. The advantage of utilizing DOE lies in its higher transmission efficiency compared to spinning disks, often exceeding 90%. This increased transmission efficiency could mitigate the intensity decrease and consequently boost the fluorescent signal.

doi:10.6342/NTU202400835

When increasing the excitation intensity, it is important to consider the tissue damage threshold due to both tissue heating and nonlinear effects in 3P microscopy. High average power might causes tissue temperature to rise, which can disrupt normal physiological functions. Additionally, high pulse energy may generate free electrons through multiphoton ionization and Zener tunneling, potentially causing sample breakdown. Therefore, it's crucial to optimize both average power and pulse energy while adhering to safety limits regarding heating and nonlinear effects.

doi:10.6342/NTU202400835

Reference List

Allen Institute for Brain Science (2004). Allen Mouse Brain Atlas. Available from https://atlas.brain-map.org/.

Araki, T. (2017). The history of optical microscope. *Mechanical Engineering Reviews* , *4* (1), 16-00242. https://doi.org/10.1299/mer.16-00242

Bando, Y., Grimm, C., Cornejo, V. H., & Yuste, R. (2019). Genetic voltage indicators. *BMC Biol 17, 71* https://doi.org/10.1186/s12915-019-0682-0

Cheng, L. C., Horton, N. G., Wang, K., Chen, S. J., & Xu, C. (2014). Measurements of multiphoton action cross sections for multiphoton microscopy. *Biomedical Optics Express* , *5* (10), 3427-3433. https://doi.org/10.1364/Boe.5.003427

Dana, H., Marom, A., Paluch, S., Dvorkin, R., Brosh, I., & Shoham, S. (2014). Hybrid multiphoton volumetric functional imaging of large-scale bioengineered neuronal networks. *Nat Commun* , *5* , 3997. https://doi.org/10.1038/ncomms4997

Diaspro, A., Chirico, G., & Collini, M. (2005). Two-photon fluorescence excitation and related techniques in biological microscopy. *Quarterly Reviews of Biophysics* , *38* (2), 97-166. https://doi.org/10.1017/S0033583505004129

Duncan, M. D., Reintjes, J., & Manuccia, T. J. (1982). Scanning Coherent Anti-Stokes Raman Microscope. *Optics Letters* , *7* , 350-352. https://doi.org/10.1364/Ol.7.000350

doi:10.6342/NTU202400835

Escobet-Montalbán, A., Gasparoli, F. M., Nylk, J., Liu, P. F., Yang, Z. Y., & Dholakia, K. (2018). Three-photon light-sheet fluorescence microscopy. *Optics Letters* , *43* (21), 5484-5487. https://doi.org/10.1364/Ol.43.005484

Freudiger, C. W., Min, W., Saar, B. G., Lu, S., Holtom, G. R., He, C. W., . . . Xie, X. S. (2008). Label-Free Biomedical Imaging with High Sensitivity by Stimulated Raman Scattering Microscopy. *Science* , *322* (5909), 1857-1861. https://doi.org/10.1126/science.1165758

Furuta, T., Yamauchi, K., Okamoto, S., Takahashi, M., Kakuta, S., Ishida, Y., . . . Hioki, H. (2022). Multi-scale light microscopy/electron microscopy neuronal imaging from brain to synapse with a tissue clearing method, ScaleSF. *iScience* , *25* (1). https://doi.org/10.1016/j.isci.2021.103601

Hodgkin, A. L., & Huxley, A. F. (1939). Action Potentials Recorded from Inside a Nerve Fibre. Nature 144, 710–711. https://doi.org/10.1038/144710a0

Hontani Y, Akbari N, Kolkman KE, Wu C, Xia F, Choe K, Wang GZ, Sokolova M, Fetcho JR, Xu C. Deep-Tissue Three-Photon Fluorescence Microscopy in Intact Mouse and Zebrafish Brain. J Vis Exp. 2022 Jan 13;(179). https://dx.doi.org/10.3791/63213.

Horton, N. G., Wang, K., Kobat, D., Clark, C. G., Wise, F. W., Schaffer, C. B., & Xu, C. (2013). *In vivo* three-photon microscopy of subcortical structures within an intact mouse brain. *Nature Photonics* , *7* (3), 205-209. https://doi.org/10.1038/Nphoton.2012.336

Hsu, K. J., Lin, Y. Y., Chiang, A. S., & Chu, S. W. (2019). Optical properties of adult Drosophila brains in one-, two-, and three-photon microscopy. *Biomed Opt Express* , *10* (4), 1627-1637. https://doi.org/10.1364/BOE.10.001627

doi:10.6342/NTU202400835

Huang, S.-H., Irawati, N., Chien, Y.-F., Lin, J.-Y., Tsai, Y.-H., Wang, P.-Y., . . . Chu, S.-W. (2021). Optical volumetric brain imaging: speed, depth, and resolution enhancement. *Journal of Physics D: Applied Physics* , *54* (32), 323002. https://doi.org/10.1088/1361-6463/abff7b

Imperato, S., Harms, F., Hubert, A., Mercier, M., Bourdieu, L., & Fragola, A. (2022). Single-shot quantitative aberration and scattering length measurements in mouse brain tissues using an extended-source Shack-Hartmann wavefront sensor. *Optics Express* , *30* (9), 15250-15265. https://doi.org/10.1364/Oe.456651

Bueno, J.M., Liao, YS., Ávila, F.J., Cheng, SF., Chu, SW. (2022). Drosophila Brain Advanced Multiphoton Imaging. In: Mazumder, N., Gangadharan, G., Kistenev, Y.V. (eds) Advances in Brain Imaging Techniques. Springer, Singapore. https://doi.org/10.1007/978-981-19-1352-5_4

Keiser, G. (2022). Light-Tissue Interactions. In G. Keiser (Ed.), *Biophotonics: Concepts to Applications* (pp. 169-221). Springer Nature Singapore. https://doi.org/10.1007/978-981-19-3482-7_6

Kennedy, D., & Norman, C. (2005). What Don't We Know? *Science* , *309* (5731), 75-75. https://doi.org/doi:10.1126/science.309.5731.75

Kobat, D., Durst, M. E., Nishimura, N., Wong, A. W., Schaffer, C. B., & Xu, C. (2009). Deep tissue multiphoton microscopy using longer wavelength excitation. *Optics Express* , *17* (16), 13354-13364. https://doi.org/10.1364/OE.17.013354

Kornfeld, J., & Denk, W. (2019). Progress and remaining challenges in high-throughput volume

doi:10.6342/NTU202400835

electron microscopy (vol 50, pg 261, 2018). *Current Opinion in Neurobiology* , *55* , 213-213. https://doi.org/10.1016/j.conb.2019.05.003

Liu, H. J., Deng, X. Q., Tong, S., He, C., Cheng, H., Zhuang, Z. W., . . . Wang, K. (2019). In Vivo Deep-Brain Structural and Hemodynamic Multiphoton Microscopy Enabled by Quantum Dots. *Nano Letters* , *19* (8), 5260-5265. https://doi.org/10.1021/acs.nanolett.9b01708

Maioli, V., Boniface, A., Mahou, P., Ortas, J. F., Abdeladim, L., Beaurepaire, E., & Supatto, W. (2020). Fast in vivo multiphoton light-sheet microscopy with optimal pulse frequency. *Biomed Opt Express* , *11* (10), 6012-6026. https://doi.org/10.1364/BOE.400113

Minsky, M. (1957). *Microscopy apparatus* . U. S. P. Office. https://worldwide.espacenet.com/textdoc?DB=EPODOC&IDX=US3013467

Müller-Wille, S. (2010). Cell theory, specificity, and reproduction, 1837-1870. *Stud Hist Philos Biol Biomed Sci* , *41* (3), 225-231. https://doi.org/10.1016/j.shpsc.2010.07.008

Oreopoulos, J., Berman, R., & Browne, M. (2014). Spinning-disk confocal microscopy: present technology and future trends. *Quantitative Imaging in Cell Biology* , *123* , 153-175. https://doi.org/10.1016/B978-0-12-420138-5.00009-4

Otomo, K., Goto, A., Yamanaka, Y., Hori, T., Nakayama, H., & Nemoto, T. (2020). High-peak-power 918-nm laser light source based two-photon spinning-disk microscopy for green fluorophores. *Biochem Biophys Res Commun* , *529* (2), 238-242. https://doi.org/10.1016/j.bbrc.2020.05.213

doi:10.6342/NTU202400835

Otomo, K., Hibi, T., Murata, T., Watanabe, H., Kawakami, R., Nakayama, H., . . . Nemoto, T. (2015). Multi-point Scanning Two-photon Excitation Microscopy by Utilizing a High-peak-power 1042-nm Laser. *Analytical Sciences* , *31* (4), 307-313. https://doi.org/10.2116/analsci.31.307

Ouzounov, D. G., Wang, T., Wang, M., Feng, D. D., Horton, N. G., Cruz-Hernandez, J. C., . . . Xu, C. (2017). In vivo three-photon imaging of activity of GCaMP6-labeled neurons deep in intact mouse brain. *Nat Methods* , *14* (4), 388-390. https://doi.org/10.1038/nmeth.4183

Petráň, M., Hadravský, M., Egger, M. D., & Galambos, R. (1968). Tandem-Scanning Reflected-Light Microscope*. *Journal of the Optical Society of America* , *58* (5), 661-664. https://doi.org/10.1364/JOSA.58.000661

Rowlands, C. J., Park, D., Bruns, O. T., Piatkevich, K. D., Fukumura, D., Jain, R. K., . . . So, P. T. C. (2017). Wide-field three-photon excitation in biological samples. *Light-Science & Applications* , *6* .https://doi.org/10.1038/lsa.2016.255

Scanziani, M., & Häusser, M. (2009). Electrophysiology in the age of light. *Nature* , *461* (7266), 930-939. https://doi.org/10.1038/nature08540

Schrodel, T., Prevedel, R., Aumayr, K., Zimmer, M., & Vaziri, A. (2013). Brain-wide 3D imaging of neuronal activity in Caenorhabditis elegans with sculpted light. *Nat Methods* , *10* (10), 1013-1020. https://doi.org/10.1038/nmeth.2637

Shimomura, O., Johnson, F. H., & Saiga, Y. (1962). Extraction, purification and properties of aequorin, a bioluminescent protein from the luminous hydromedusan, Aequorea. *J Cell*

doi:10.6342/NTU202400835

Comp Physiol , *59* , 223-239. https://doi.org/10.1002/jcp.1030590302

Shimozawa, T., Yamagata, K., Kondo, T., Hayashi, S., Shitamukai, A., Konno, D., . . . Mimori-Kiyosue, Y. (2013). Improving spinning disk confocal microscopy by preventing pinhole cross-talk for intravital imaging. *Proc Natl Acad Sci U S A* , *110* (9), 3399-3404. https://doi.org/10.1073/pnas.1216696110

Sigal, Y. M., Zhou, R. B., & Zhuang, X. W. (2018). Visualizing and discovering cellular structures with super-resolution microscopy. *Science* , *361* (6405), 880-887. https://doi.org/10.1126/science.aau1044

Streich, L., Boffi, J. C., Wang, L., Alhalaseh, K., Barbieri, M., Rehm, R., . . . Prevedel, R. (2021). High-resolution structural and functional deep brain imaging using adaptive optics three-photon microscopy. *Nature Methods* , *18* (10), 1253-+. https://doi.org/10.1038/s41592-021-01257-6

Takasaki, K., Abbasi-Asl, R., & Waters, J. (2020). Superficial Bound of the Depth Limit of Two-Photon Imaging in Mouse Brain. *Eneuro* , *7* (1). https://doi.org/10.1523/eneuro.0255-19.2019

Truong, T. V., Supatto, W., Koos, D. S., Choi, J. M., & Fraser, S. E. (2011). Deep and fast live imaging with two-photon scanned light-sheet microscopy. *Nat Methods* , *8* (9), 757-760. https://doi.org/10.1038/nmeth.1652

Wang, M. R., Wu, C. Y., Sinefeld, D., Li, B., Xia, F., & Xu, C. (2018).Comparing the effective attenuation lengths for long wavelength *in vivo* imaging of the mouse brain *Biomedical Optics Express* , *9* (8). https://doi.org/10.1364/BOE.9.003534

doi:10.6342/NTU202400835

Wang, T., Ouzounov, D. G., Wang, M., & Xu, C. (2017, 2017/04/02). Quantitative Comparison of Two-photon and Three-photon Activity Imaging of GCaMP6s-labeled Neurons in vivo in the Mouse Brain. *OSA Technical Digest (online)* Optics in the Life Sciences Congress. https://doi.org/10.1364/BRAIN.2017.BrM4B.4

Wang, T. Y., Wu, C. Y., Ouzounov, D. G., Gu, W. C., Xia, F., Kim, M., . . . Xu, C. (2020). Quantitative analysis of 1300-nm three-photon calcium imaging in the mouse brain. *eLife 9:e53205.*. https://doi.org/10.7554/eLife.53205

Weisenburger, S., Tejera, F., Demas, J., Chen, B., Manley, J., Sparks, F. T., . . . Vaziri, A. (2019). Volumetric Ca2+ Imaging in the Mouse Brain Using Hybrid Multiplexed Sculpted Light Microscopy. *Cell* , *177* (4),1050-1066.e14. https://doi.org/10.1016/j.cell.2019.03.011

Whittaker, E. T. (2018). *A History of the Theories of Aether and Electricity from the Age of Descartes to the Close of the Nineteenth Century* . Creative Media Partners, LLC.

Wolf, S., Supatto, W., Debregeas, G., Mahou, P., Kruglik, S. G., Sintes, J. M., . . . Candelier, R. (2015). Whole-brain functional imaging with two-photon light-sheet microscopy. *Nat Methods* , *12* (5), 379-380. https://doi.org/10.1038/nmeth.3371

Wu, J., Ji, N., & Tsia, K. K. (2021). Speed scaling in multiphoton fluorescence microscopy. *Nature Photonics* , *15* (11), 800-812. https://doi.org/10.1038/s41566-021-00881-0

Xiao, G. Q., Corle, T. R., & Kino, G. S. (1988). Real-Time Confocal Scanning Optical Microscope. *Applied Physics Letters* , *53* (8), 716-718. https://doi.org/10.1063/1.99814

doi:10.6342/NTU202400835

Xiao, Y., Deng, P., Zhao, Y., Yang, S., & Li, B. (2023). Three-photon excited fluorescence imaging in neuroscience: From principles to applications [Review]. *Frontiers in Neuroscience* , *17* . https://doi.org/10.3389/fnins.2023.1085682

Zernike, F. (1942). Phase contrast, a new method for the microscopic observation of transparent objects. *Physica* , *9* (7), 686-698. https://doi.org/https://doi.org/10.1016/S0031-8914(42)80035-X

Zhang, T., Hernandez, O., Chrapkiewicz, R., Shai, A., Wagner, M. J., Zhang, Y., . . . Schnitzer, M. J. (2019). Kilohertz two-photon brain imaging in awake mice. *Nat Methods* , *16* (11), 1119-1122. https://doi.org/10.1038/s41592-019-0597-2

Zhang, Y., Rózsa, M., Liang, Y. J., Bushey, D., Wei, Z. Q., Zheng, J. H., . . . Looger, L. L. (2023). Fast and sensitive GCaMP calcium indicators for imaging neural populations. *Nature* , *615* (7954), 884-+. https://doi.org/10.1038/s41586-023-05828-9

Zheng, Z. H., Lauritzen, J. S., Perlman, E., Robinson, C. G., Nichols, M., Milkie, D., . . . Bock, D. D. (2018). A Complete Electron Microscopy Volume of the Brain of Adult. *Cell* , *174* (3), 730-+. https://doi.org/10.1016/j.cell.2018.06.019

doi:10.6342/NTU202400835